Moderately Rough Surface Underground Imaging via Short-Pulse Quasi-Ray Gaussian Beams

Vincenzo Galdi, *Member, IEEE*, Haihua Feng, *Member, IEEE*, David A. Castañon, *Senior Member, IEEE*, William Clem Karl, *Senior Member, IEEE*, and Leopold B. Felsen, *Life Fellow, IEEE*

***Abstract*—An adaptive framework is presented for ultra-wideband ground penetrating radar imaging of shallowly-buried low-contrast dielectric objects in the presence of a moderately rough air-soil interface. The proposed approach works with sparse data and relies on recently developed Gabor-based narrow-waisted quasi-ray Gaussian beam algorithms as fast forward scattering predictive models. First, a nonlinear inverse scattering problem is solved to estimate the unknown coarse-scale roughness profile. This sets the stage for adaptive compensation of clutter-induced distortion in the underground imaging problem, which is linearized via Born approximation and subsequently solved via various *pixel-based* and *object-based* techniques. Numerical simulations are presented to assess accuracy, robustness and computational efficiency for various calibrated ranges of problem parameters. The proposed approach has potential applications to antipersonnel land mine remediation.**

***Index Terms*—Curve evolution, Gaussian beams, ground penetrating radars, rough surfaces, short pulses, total variation.**

I. Introduction

THE problem of detecting and localizing buried objects via ground penetrating radar (GPR) has received considerable attention in recent years, with potential applications ranging from nondestructive testing to environmental remediation. In this context, one of the most important and difficult applications is related to the clearance of buried unexploded ordinance, such as plastic antipersonnel land mines [1]. Attacking such a problem requires a judicious blend of efficient physics-based modeling and advanced signal processing. The associated electromagnetic (EM) model involves wave propagation in inhomogeneous, lossy, dispersive media, and "near-field" scattering from irregularly-shaped objects and interfaces. From a signal processing perspective, the main challenges are related to the limited-viewing geometry, the low permittivity contrast of the target with respect to the background soil (i.e., low signal-to-noise ratio), the imperfect knowledge of geometric and constitutive properties of soil and targets, and the possible presence of clutter which obscures the useful signals. In particular, the effect of the rough air-ground interface, in terms of backscattered clutter and distortion introduced into the interrogating signal on its way to and from the targets of interest, is a key issue from both the EM and signal processing perspectives. In this connection, standard approaches tend to be *fully statistical*, modeling such effects as additive colored Gaussian noise whose features are typically estimated via full-wave Monte Carlo simulations with many random soil realizations. These approaches have been explored in [2]–[5], yielding reasonably good results for the *detection* problem in the presence of small roughness. However, their accuracy and reliability turn out to be not completely satisfactory in underground imaging algorithms aimed at *localizing* and possibly *classifying* a target (see, e.g., [6]).

In an ongoing series of recent investigations, so far restricted to two-dimensional (2-D) geometries and moderate roughness, we have been exploring a novel *adaptive* framework, based on prior estimation of the unknown coarse scale roughness profile and subsequent compensation for the deterministic features of the related clutter. In a stepwise approach toward constructing the necessary tools, in both the frequency (FD) and time (TD) domains, we first developed physics-based fast forward algorithms for scattering from, and transmission through, moderately rough dielectric interfaces, generalizing previously developed Gabor-based narrow-waisted (NW) quasi-ray Gaussian beam (GB) methods [7]–[9]. The resulting FD/TD Gabor-based GB models in [10], [11] have subsequently been incorporated in inverse scattering scenarios aimed at enhancing the underground imaging by compensating for the coarse scale deterministic features of the roughness profile. In particular, FD and TD surface estimation algorithms working with sparse data have been explored in [12] and [13], respectively. These techniques were found to provide reasonably accurate and robust estimations, even with noisy data and imperfect knowledge of soil parameters, requiring modest computational effort. Applications to frequency-stepped GPR subsurface imaging have been explored in [14].

The present paper is concerned with the application of the Gabor-based physical-optics pulsed-beam (PO-PB) forward scattering model in [11] and the surface estimation technique in [13] to the imaging of shallowly-buried plastic mine-like targets

Manuscript received October 30, 2001; revised July 12, 2002. This work was supported by ODDR&E under MURI Grants ARO DAAG55-97-1-0013 and AFOSR F49620-96-1-0028, and by the Engineering Research Centers Program of the National Science Foundation under award number EEC-9986821. The work of V. Galdi was also supported by a European Union postdoctoral fellowship through the University of Sannio, Benevento, Italy. L. B. Felsen also acknowledges partial support from Grant No. 9900448 by the US-Israel Binational Science Foundation, Jerusalem, Israel, and from Polytechnic University, Brooklyn, NY 11201 USA.

V. Galdi is with the Waves Group, Department of Engineering, University of Sannio, I-82100 Benevento, Italy (e-mail: vgaldi@unisannio.it).

H. Feng is with The MathWorks Incorporated, Natick, MA 01760 USA (e-mail: hfeng@mathworks.com).

D. A. Castañon and W. C. Karl are with the Multi-Dimensional Signal Processing Laboratory, Department of Electrical and Computer Engineering, Boston University, Boston, MA 02215 USA (e-mail: dac@bu.edu; wckarl@bu.edu).

L. B. Felsen is with the Department of Aerospace and Mechanical Engineering and the Department of Electrical and Computer Engineering, Boston University, Boston, MA 02215 USA, part-time. He is also University Professor Emeritus, Polytechnic University, Brooklyn, NY 11201 USA (e-mail: lfelsen@bu.edu).

Digital Object Identifier 10.1109/TAP.2003.816363

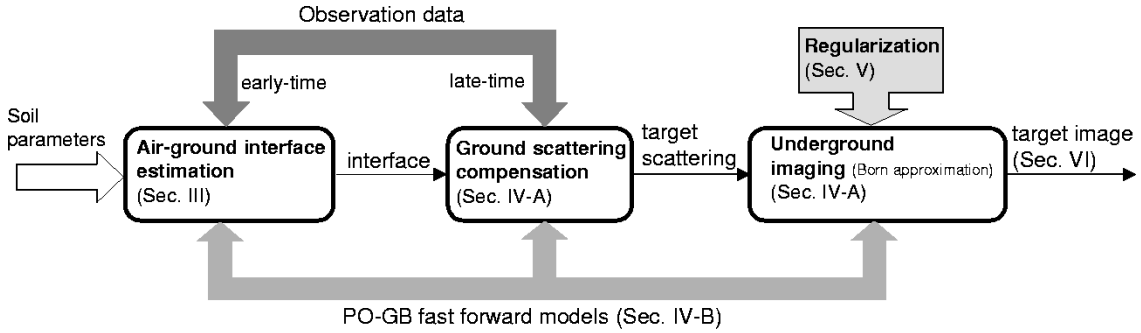

Fig. 1. Schematic flow-chart of the proposed adaptive approach, coordinated with the paper layout.

in the presence of rough air-soil interfaces, working with TD sparse data. Many GPR systems operate with short-pulse excitation. Although one could still process the data in the FD via Fourier transform, a *direct* approach in the TD offers potential advantages, including the possibility of carrying out *selective* imaging via suitable *time-windowing* of the data. Accordingly, in our problem, we shall exploit the (usually small) separation between the rough interface and the target by performing first the surface estimation via early-time response processing (as discussed in [13]), with subsequent compensation for the roughness effect and eventual target imaging via late-time response processing. In this connection, we shall utilize the weak-scattering Born approximation to linearize the inversion problem, and explore various regularization techniques to cope with its inherent ill-posedness. Fig. 1 shows a schematic flow-chart of the proposed framework, coordinated with the paper layout, which illustrates how the various models and techniques described in the paper are combined to attack the end-to-end problem.

Implementation of the proposed synthetic problem strategy, based on the interactive combination of previously explored model constituents, is subject to particular constraints which are dealt with in detail in Section VI. Loosely speaking, we consider shallowly-buried, low-contrast targets in the presence of moderate interface roughness. The high-frequency asymptotic FD halfspace Green's function in the presence of the moderately rough interface, as well as the interface-transmitted field, are parameterized in terms of a superposition of paraxially approximated Gabor NW-GBs launched by the equivalent PO "currents" on the interface profile. The implied restriction to the "paraxial far zone" of the individual GBs excludes source points and observation points close to the interface which, together with other inherent signal processing limitations, imposes constraints on the minimum allowable depth of a buried target, and therefore on the ability, in the TD, to allow the selective interface/target imaging via early-time and late-time processing, respectively. Although the shallow target depth in our synthetic numerical experiments appears to violate weakly some of these fovsk —9rmal constraints, we have found the final reconstructions to be remarkably insensitive to these and other imperfections over a calibrated range of problem parameters. The same is true when the observation data is corrupted by noise or small errors in the "known" forward model.

Concerning the novelty of our overall problem strategy, we are not aware of *direct* TD algorithms which address this difficult imaging problem.

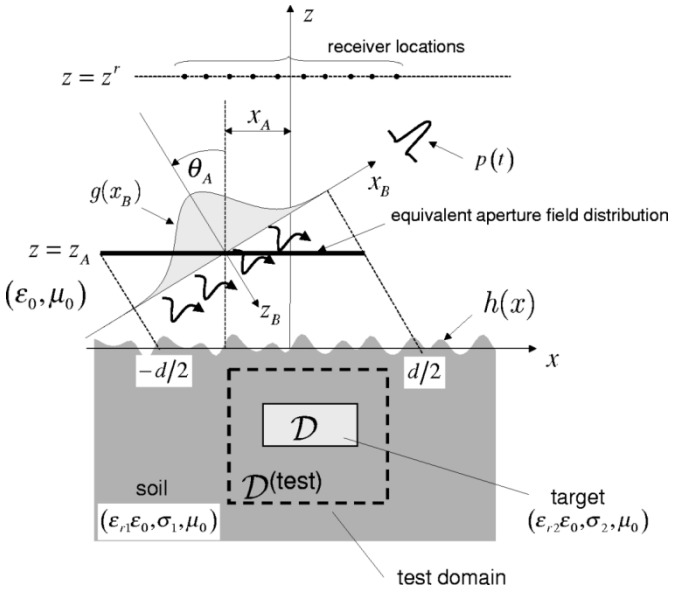

Fig. 2. Problem geometry. An aperture-generated, quasi-plane-wave, TM-polarized pulsed field impinges from free space onto a homogeneous dielectric halfspace with known relative permittivity ϵ_{r1} and conductivity σ_1, bounded by a moderately rough interface profile $z = h(x)$, wherein a homogeneous dielectric target with relative permittivity ϵ_{r2} and conductivity $\sigma_2 \approx 0$ occupies the region $\mathcal{D}$. In order to image the test domain $\mathcal{D}^{(\text{test})}$, the reflected field is sampled at N_t time instants at N_r fixed receiver locations $x_1^r, \ldots, x_{N_r}^r$ on the observation plane $z = z^r$.

The layout of the paper is as follows. Section II introduces the rough surface underground imaging problem with TD GPR sparse data. Section III gives a short review of the surface estimation algorithm in [13]. Section IV describes the linearized forward scattering model in the presence of a *known* rough interface, and its NW-GB implementation. Section V addresses the underground imaging inversion problem and the various regularization techniques explored. Section VI details the outcomes of numerical experiments to assess the accuracy and reliability of the proposed approach, as well as its computational efficiency. Conclusions follow in Section VII.

II. Statement of the Problem

The problem geometry is sketched in Fig. 2: In an (x, z) 2-D coordinate space, a homogeneous dielectric target with relative permittivity ϵ_{r2} and negligible conductivity σ_2 is buried in a lossy homogeneous dielectric halfspace (soil) of known relative permittivity ϵ_{r1} and weak conductivity σ_1, bounded by a moderately rough interface with profile $z = h(x)$. The target region in

the halfspace $z < h(x)$ is denoted by $\mathcal{D}$. As stated previously, we are mainly interested in shallowly-buried plastic mine-like targets, which are essentially lossless ($\sigma_2 \approx 0$) and may have dielectric properties very close to those of the background soil, i.e., $|\epsilon_{r2} - \epsilon_{r1}|/\epsilon_{r1} \ll 1$. In what follows, the wavenumbers in free space and soil will be denoted by $k_0 = \omega\sqrt{\epsilon_0\mu_0}$ and $k_1 = k_0\sqrt{\epsilon_{r1} + i\sigma_1/(\omega\epsilon_0)}$, respectively, with ω representing the angular frequency, and ϵ_0, μ_0 denoting the free-space permittivity and permeability, respectively.

The soil is illuminated by a y-directed (TM-polarized) pulsed field generated by a (projected) large truncated aperture field distribution of width d at $z = z_A$. As typical of many ultra-wideband (UWB) GPR systems, we assume that the incident field is sufficiently well-collimated so that it can be approximated by a pulsed truncated tapered plane wave

$$e^i(\mathbf{r}, t) \sim g(x_B)p(t - c^{-1}z_B) \tag{1}$$

with FD spectrum

$$E^i(\mathbf{r}, \omega) \sim g(x_B)P(\omega)\exp(ik_0 z_B). \tag{2}$$

In (1) and (2), $\mathbf{r} \equiv (x, z)$, $p(t)$ is a short pulse of length $T \ll d/c$ with FD spectrum $P(\omega)$, $c = (\epsilon_0\mu_0)^{-1/2}$ is the free-space wavespeed, $g(x_B)$ is a spatial taper, and (x_B, z_B) are beam centered coordinates

$$\begin{bmatrix} x_B \\ z_B \end{bmatrix} = \begin{bmatrix} \cos\theta_A & \sin\theta_A \\ \sin\theta_A & -\cos\theta_A \end{bmatrix} \begin{bmatrix} x - x_A \\ z - z_A \end{bmatrix} \tag{3}$$

with θ_A and x_A denoting the tilt angle of the radiated beam relative to the z axis and its spatial displacement, respectively. Parameters are chosen so that the illumination tapers to zero for $|x| \leq d/2$ and vanishes for $|x| > d/2$ (Fig. 2). Here and henceforth, capital letters identify FD quantities, whereas lower case letters are used for TD quantities; FD and TD quantities are related through the following Fourier transform pair

$$\begin{aligned} f(\mathbf{r}, t) &= \frac{1}{2\pi}\int_{-\infty}^{\infty} F(\mathbf{r}, \omega)\exp(-i\omega t)d\omega \\ F(\mathbf{r}, \omega) &= \int_{-\infty}^{\infty} f(\mathbf{r}, t)\exp(i\omega t)dt. \end{aligned} \tag{4}$$

Apart from the presence of the target, the geometry and notation are the same as in [11] and [13], to which we shall refer frequently throughout the paper. Notationally, we shall use $(\alpha.\beta)$ to denote equation (β) in reference $[\alpha]$; for instance, (3.8) means (8) in [3]. As in [11] and [13], the soil is assumed to be slightly lossy, i.e., $\sigma_1 \ll \Omega_0\epsilon_0\epsilon_{r1}$, with Ω_0 denoting the effective bandwidth of the pulse $P(\omega)$.

The actual goal of this investigation is the *imaging* of an underground test domain (e.g., $\mathcal{D}^{(\text{test})}$ in Fig. 2), i.e., the estimation, from sparse TD scattered field observations, of its dielectric properties in order to localize and classify possible anomalies. To this end, the y-directed scattered electric field is sampled at N_t time instants at N_r fixed receiver locations $x_1^r, \ldots, x_{N_r}^r$ on the plane $z = z^r$ (Fig. 2) to obtain a set of observations. The *known term* in the problem is this set of $N_r \times N_t$ samples. In our numerical experiments in Section VI, we shall use synthetic field observation data generated via a *rigorous full-wave solution* of the forward scattering problem (see Section VI-A), which accounts for *all* interface/target interactions.

III. Rough Surface Profile Estimation

In principle, the problem of estimating the coarse-scale roughness profile of the air-ground interface can be addressed with various technologies (e.g., acoustics, laser, SAR, etc.). In [13], we proposed a simple strategy based on the processing of the *early-time* response of a UWB GPR system sampled at a limited number of receivers. Our approach is based on a compact low-dimensional spline parameterization of the roughness profile, which provides implicit regularization mitigating the inherent ill-posedness of the problem, and on the PO-PB forward scattering model in [11] to generate predictions of the reflected field at the receivers. The estimation problem is thus converted into a nonlinear optimization problem aimed at retrieving the unknown spline coefficients via minimization of a least-square error functional that involves the PO-PB forward scattering prediction and the available observed data. The observation time windows are chosen so as to gate out the *late-time* response (i.e., causal contributions from regions beyond a critical depth) due to the possible presence there of buried targets which may produce a bias in the surface estimation. The resulting optimization problem is generally *nonconvex*, and therefore the possible presence of local minima renders its numerical implementation nontrivial. Optimization strategies and computational issues are discussed in [13]. The proposed approach was found to provide accurate and robust estimations (even with noisy data and imperfect knowledge of soil parameters) with mild computational effort (typical computing time $\sim$55 secs. on a 700 MHz PC).

Having established the possibility of estimating the coarse shape of the rough air-ground interface via *early-time* response processing, we now turn to the problem of underground imaging in the presence of a *known* moderately rough interface. In our investigation, incoherent scattering contributions from finer-scale roughness are not included. These finer-scale contributions are effectively dealt with through the use of additive noise models.

IV. Forward Scattering Model

A. Formulation

Referring to Fig. 2, the y-directed TM-polarized *total* FD field observed in free space at $\mathbf{r} = (x, z)$ can be conveniently expressed as a sum of two components—the target scattering contribution E^s and the *background field* E^b (i.e., the field in the absence of the target)

$$E(\mathbf{r}, \omega) = E^b(\mathbf{r}, \omega) + E^s(\mathbf{r}, \omega) \tag{5}$$

with E^s given by [15]

$$E^s(\mathbf{r}, \omega) = \frac{\omega^2}{c^2}\int\!\!\int_{\mathcal{D}} E(\mathbf{r}', \omega)G_b(\mathbf{r}, \mathbf{r}', \omega)O(\mathbf{r}', \omega)d\mathbf{r}'. \tag{6}$$

In (6), E is the *total* field in the target region, G_b represents the FD Green's function of the rough-interface dielectric halfspace, and

$$O(\mathbf{r}',\omega)=[\epsilon_r(\mathbf{r}')-\epsilon_{r1}]+i\frac{[\sigma(\mathbf{r}')-\sigma_1]}{\omega\epsilon_0}=\Delta\epsilon_r(\mathbf{r}')+i\frac{\Delta\sigma(\mathbf{r}')}{\omega\epsilon_0} \tag{7}$$

is usually referred to as the *object function*, with $\epsilon_r(\mathbf{r}')$ and $\sigma(\mathbf{r}')$ denoting the local relative dielectric permittivity and conductivity, respectively. Since the object function in (7) vanishes outside the target region $\mathcal{D}$,the integration in (6) is limited accordingly. The corresponding TD results, of interest in this paper, are obtained by Fourier inversion of (5) and (6),

$$e(\mathbf{r},t)=e^b(\mathbf{r},t)+e^s(\mathbf{r},t) \tag{8}$$

where

$$e^b(\mathbf{r},t)=\frac{1}{2\pi}\int_{-\infty}^{\infty}E^b(\mathbf{r},\omega)\exp(-i\omega t)d\omega \tag{9}$$

$$e^s(\mathbf{r},t)=\int\int_{\mathcal{D}}\Delta\epsilon_r(\mathbf{r}')u(\mathbf{r},\mathbf{r}',t)d\mathbf{r}' + \frac{1}{c\epsilon_0}\int\int_{\mathcal{D}}\Delta\sigma(\mathbf{r}')v(\mathbf{r},\mathbf{r}',t)d\mathbf{r}'. \tag{10}$$

The kernels u and v in (10) are given by

$$u(\mathbf{r},\mathbf{r}',t)=\frac{1}{2\pi c^2}\int_{-\infty}^{\infty}\omega^2E(\mathbf{r}',\omega)G_b(\mathbf{r},\mathbf{r}',\omega)\exp(-i\omega t)d\omega \tag{11}$$

$$v(\mathbf{r},\mathbf{r}',t)=\frac{1}{2\pi c}\int_{-\infty}^{\infty}i\omega E(\mathbf{r}',\omega)G_b(\mathbf{r},\mathbf{r}',\omega)\exp(-i\omega t)d\omega. \tag{12}$$

Thus, in the total backscattered field (8) observed at the receivers, e^s is the *useful* signal carrying the information needed for imaging the target, whereas e^b is the interface-generated clutter. Further distortion introduced in the useful signal by the twice-traversed rough air-ground interface is accounted for in the fields E and G_b in (11) and (12). Assuming that an estimation of the rough interface profile is somehow available, one can use a full-wave forward solver, or the more efficient PO-PB forward scattering model in [11], to generate a prediction of the clutter e^b in (8) for a given pulsed excitation, and therefore *isolate* the target contribution e^s. Even removing the background clutter e^b, the relation in (10) between the scattered field at the receivers and the permittivity and conductivity contrasts $\Delta\epsilon_r$ and $\Delta\sigma$ is not easily invertible, due to the presence in (11) and (12) of the total field E which is itself dependent on $\Delta\epsilon_r$ and $\Delta\sigma$ and consequently renders the problem *nonlinear*. However, for the plastic anti-personnel land mines of interest here, with dielectric properties close to those of the background soil, one can invoke the weak scattering limit via use of the Born approximation [15], where the total field E inside the target is replaced by the transmitted field E^t in $\mathcal{D}$, in the absence of the target. Moreover, we shall neglect the conductivity contrast contribution in (10), thus arriving at a *linear* model relating the scattered field at the receivers to the relative permittivity contrast $\Delta\epsilon_r$

$$e^s(\mathbf{r},t)\approx\int\int_{\mathcal{D}}\Delta\epsilon_r(\mathbf{r}')\bar{u}(\mathbf{r},\mathbf{r}',t)d\mathbf{r}' \tag{13}$$

$$\bar{u}(\mathbf{r},\mathbf{r}',t)=\frac{1}{2\pi c^2}\int_{-\infty}^{\infty}\omega^2E^t(\mathbf{r}',\omega)G_b(\mathbf{r},\mathbf{r}',\omega)\times\exp(-i\omega t)d\omega. \tag{14}$$

The robust inversion of this model will be discussed in Section V. The limitations of the Born approximation, which neglects multibounce interactions inside the target, have been thoroughly investigated and are well documented in the technical literature (see, e.g., [16]). More sophisticated and accurate nonlinear [17], [18], iterative [19] and distorted [20] variants could be exploited in principle, but this is outside the scope of the present investigation. For moderately lossy soils, once a first estimate of $\Delta\epsilon_r$ (and hence of $\mathcal{D}$) is obtained by inverting the linear model in (13) (see Section V), one can iteratively refine this estimate by re-introducing into (13) the neglected (Born-approximated) conductivity contribution in (10) as a *known term*.

B. Narrow-Waisted Gaussian Beam Implementation

In order to implement, and eventually invert, the TD linear model in (13) for the pulsed excitation in (1) and (2), one needs to compute the TD kernel $\bar{u}$ in (14) at several observation points for a large number of source positions and time instants, with typical total number $\sim 10^6$ (see Section VI-D. As a consequence, the availability of a fast forward solver is a key ingredient for the overall computational feasibility of the proposed approach. In this scenario, the computational burdens of typical full-wave solvers (e.g., moment methods or finite differences) tend to be prohibitive, and it is therefore suggestive to resort to approximate approaches. We found that the Gabor-based PO-PB algorithms in [11] are remarkably well-suited for this problem, and that they provide a reasonable tradeoff between accuracy and computational burden. The PO-PB synthesis of plane-wave-excited fields transmitted into a rough-surface homogeneous halfspace detailed in [11] can readily be extended to the deal with the subsequent irradiation from an induced line-source in the dielectric halfspace, thereby yielding a *closed form* TD expression for the kernel in (14) similar to those in [11]. However, for reasons that will become clear later on (Section IV-B-3), it is computationally cheaper to synthesize the transmitted field E^t and the rough-surface halfspace Green's function G_b in the FD, and then compute the TD kernel in (14) via fast Fourier transform (FFT) algorithms [21].

1) Transmitted Field: The computation of the field transmitted into the halfspace $z<h(x)$ in the absence of the target, under the quasi-plane-wave pulsed illumination in (2), is a problem already addressed in [11]. We therefore merely cite the final results, referring the reader to [11] for theoretical and computational details. The FD PO "equivalent current," which generates the transmitted field, is parameterized in terms of x-domain discretized m_1-indexed Gabor basis functions with

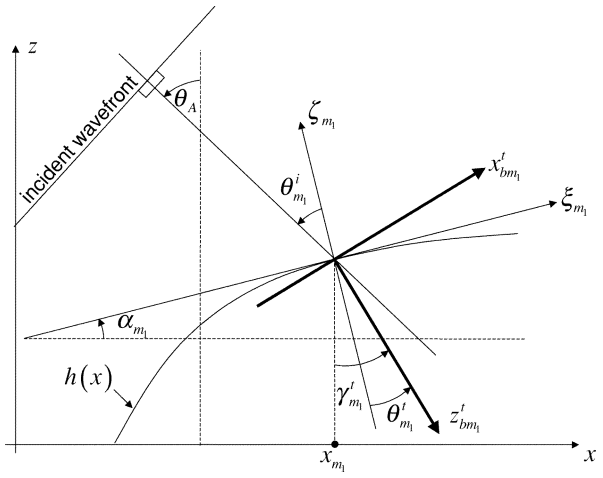

Fig. 3. Global and local coordinates for beams transmitted from free space into the soil. $(x^t_{bm_1}, z^t_{bm_1})$ is the m_1th transmitted-beam-centered local coordinate system; (ξ_{m_1}, ζ_{m_1}) is the local tangent-normal coordinate system, centered at lattice points $(x_{m_1}, h(x_{m_1}))$; $\alpha_{m_1} = \tan^{-1}[dh(x_{m_1})/dx]$ is the local slope; $\theta^t_{m_1}$ is the local refraction angle measured from the surface normal; $\gamma^t_{m_1} = \theta^t_{m_1} + \alpha_{m_1}$ is the local refraction angle measured from the z axis.

narrow width $L_1 \lesssim |\lambda_1| \ll d$, centered on the Gabor lattice points $x_{m_1} = m_1 L_1$, with $\lambda_1 = 2\pi/k_1$ denoting the wavelength in soil. These initial conditions generate narrow-waisted (NW) quasi-ray GBs propagating along the local refraction directions (Fig. 3). One obtains the following FD synthesis [cf. (11.21) and (11.22)]

$$E^t(\mathbf{r},\omega) \sim \frac{1}{2} \sum_{|m_1| \le \left(\frac{d}{2L_1}\right)} C^t_{m_1}(\omega) \tilde{\mathcal{B}}^t_{m_1}(\mathbf{r},\omega) \tag{15}$$

where the Gabor coefficients $C^t_{m_1}$ can be estimated efficiently by sampling the PO "equivalent current" at the lattice points x_{m_1}

$$C^t_{m_1}(\omega) \approx 2\left(\frac{L_1}{\sqrt{2}}\right)^{\frac{1}{2}} g(x_{Bm_1}) \left[1 + \mathcal{R}^{(1)}_{m_1}\right] \times P(\omega) \exp\left[ik_0\left(z_{Bm_1} - x_{m_1}\frac{\sin\theta^i_{m_1}}{\cos\alpha_{m_1}}\right)\right]. \tag{16}$$

In (16), (x_{Bm_1}, z_{Bm_1}) denote the lattice points $(x_{m_1}, h(x_{m_1}))$ in the incident-beam coordinates (3), $\alpha_{m_1} = \tan^{-1}[dh(x_{m_1})/dx]$ is the local surface slope, $\theta^i_{m_1} = \theta_A - \alpha_{m_1}$ is the local incidence angle (see Fig. 3), and $\mathcal{R}^{(1)}_{m_1}$ is the local Fresnel TM plane-wave reflection coefficient for incidence from free space

$$\mathcal{R}^{(1)}_{m_1} = \frac{\cos\theta^i_{m_1} - \left(\epsilon_{r1} - \sin^2\theta^i_{m_1}\right)^{\frac{1}{2}}}{\cos\theta^i_{m_1} + \left(\epsilon_{r1} - \sin^2\theta^i_{m_1}\right)^{\frac{1}{2}}}. \tag{17}$$

In (15), $\tilde{\mathcal{B}}^t_{m_1}$ is the complex-source-point (CSP) NW-GB propagator, which can be computed efficiently via CSP paraxial asymptotics [cf. (11.30)–(11.34)]

$$\tilde{\mathcal{B}}^t_{m_1}(\mathbf{r},\omega) \sim ik_1 2^{\frac{5}{4}} \left(\frac{L_1}{8\pi k_1}\right)^{\frac{1}{2}} \frac{\left(\zeta_{m_1} - ib^t_{m_1}\cos\theta^t_{m_1}\right)}{\left(\tilde{R}^t_{m_1}\right)^{\frac{3}{2}}} \times \exp\left\{i\left[k_1\left(\tilde{R}^t_{m_1} + x_{m_1}\frac{\sin\theta^t_{m_1}}{\cos\alpha_{m_1}} + ib^t_{m_1}\right) + \frac{\pi}{4}\right]\right\} \tag{18}$$

where $\theta^t_{m_1}$ is the local refraction angle (see Fig. 3), related to $\theta^i_{m_1}$ and ϵ_{r1} via Snell's law $\sin\theta^i_{m_1} = \sqrt{\epsilon_{r1}}\sin\theta^t_{m_1}$, $\zeta_{m_1} = -(x - x_{m_1})\sin\alpha_{m_1} + [z - h(x_{m_1})]\cos\alpha_{m_1}$, and $\tilde{R}^t_{m_1}$ denotes the *complex distance*

$$\tilde{R}^t_{m_1} = \sqrt{\left(x^t_{bm_1}\right)^2 + \left(z^t_{bm_1} - ib^t_{m_1}\right)^2}, \mathrm{Re}\left(\tilde{R}^t_{m_1}\right) \ge 0 \tag{19}$$

with

$$\begin{bmatrix} x^t_{bm_1} \\ z^t_{bm_1} \end{bmatrix} = \begin{bmatrix} \cos\gamma^t_{m_1} & \sin\gamma^t_{m_1} \\ \sin\gamma^t_{m_1} & -\cos\gamma^t_{m_1} \end{bmatrix} \begin{bmatrix} x - x_{m_1} \\ z - h(x_{m_1}) \end{bmatrix}$$

$$\gamma^t_{m_1} = \theta^t_{m_1} + \alpha_{m_1} \tag{20}$$

$$b^t_{m_1} = \frac{\sqrt{\epsilon_{r1}}\left(L_1\cos\alpha_{m_1}\cos\theta^t_{m_1}\right)^2}{\lambda_0}. \tag{21}$$

In (21), $\lambda_0 = 2\pi/k_0$ denotes the free-space wavelength. Moreover, the tilde $\tilde{}$ denotes quantities extended into complex coordinate space via the CSP method. Note that the CSP GB paraxial asymptotics restricts the observation range to points located more than a wavelength, or so, away from the interface. In our numerical implementation, we found reasonably accurate syntheses with beam spacing $L_1 \sim |\lambda_1|/2$. The resulting computational burden (see Section VI-E) was found to be about 2 times lower than the quasi-real ray-tracing scheme in [10], and about 4 times lower than standard Kirchhoff-PO implementations.

2) Rough-Surface Halfspace Green's Function: The next step is the Gabor-based NW-GB synthesis of the rough-surface halfspace Green's function G_b, which, in our TD-Born model in (13) and (14), represents the scattering contribution from a (infinitesimal) pixel in the target region of Fig. 2. Thus, instead of a quasi-plane-wave pulsed illumination from free space as in Section IV-B-1, we now have cylindrical waves impinging from underground induced source points $\mathbf{r}'$

$$G_1(\mathbf{r},\mathbf{r}',\omega) = -\frac{i}{4}\mathrm{H}^{(1)}_0\left(k_1|\mathbf{r} - \mathbf{r}'|\right), \quad \mathbf{r}' \in \mathcal{D} \tag{22}$$

with $\mathrm{H}^{(1)}_0(\cdot)$ denoting the zeroth order Hankel function of the first kind. As in [11, Sec. III-A], the field radiated into the halfspace $z > h(x)$ is generated by an induced PO "surface current" [cf. (11.16)]

$$J^g_{PO}(x,\mathbf{r}',\omega) = 2G_1(\mathbf{r}_h,\mathbf{r}',\omega)\left[1 + \mathcal{R}^{(2)}(x)\right], \ \mathbf{r}_h \equiv (x, h(x)) \tag{23}$$

where $\mathcal{R}^{(2)}(x)$ denotes the local Fresnel TM plane-wave reflection coefficient for incidence from soil

$$\mathcal{R}^{(2)}(x) = \frac{\sqrt{\epsilon_{r1}}\cos\alpha(x) - \left[1 - \epsilon_{r1}\sin^2\alpha(x)\right]^{\frac{1}{2}}}{\sqrt{\epsilon_{r1}}\cos\alpha(x) + \left[1 - \epsilon_{r1}\sin^2\alpha(x)\right]^{\frac{1}{2}}} \tag{24}$$

with $\alpha(x) = \tan^{-1}[dh(x)/dx]$ being the local slope (Fig. 4). This asymptotic ray model implies that the virtual line source location must be "sufficiently far" away from the interface. As in [11, Sec. III-B], it is expedient to rewrite the PO current by separating out the locally linear phase term that an incident plane wave propagating along the positive z direction would induce on the locally tangent plane [cf. (11.17)]

$$J^g_{PO}(x,\mathbf{r}',\omega) = \mathcal{J}^g_{PO}(x,\mathbf{r}',\omega)\exp\left[-ik_1 x\tan\alpha(x)\right]. \tag{25}$$

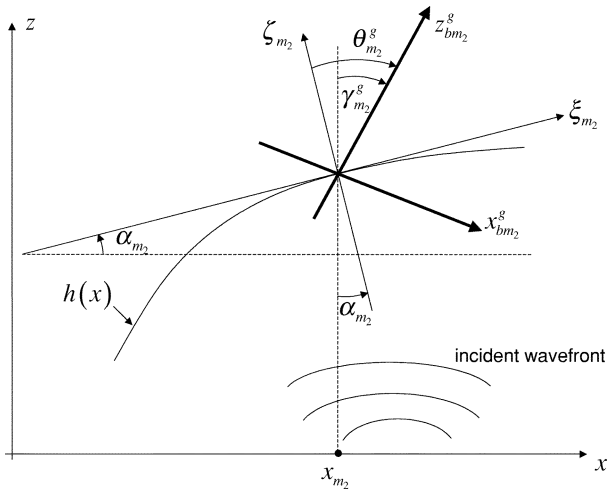

Fig. 4. As in Fig. 3, but for beams transmitted from soil into free space, with planar approximation of the incident cylindrical wavefront in (22). $(x^g_{bm_2},\ z^g_{bm_2})$ is the m_2th transmitted-beam-centered local coordinate system; $\theta^g_{m_2}$ is the local refraction angle measured from the surface normal; $\gamma^g_{m_2} = \theta^g_{m_2} - \alpha_{m_2}$ is the local refraction angle measured from the z axis.

By Gabor-expanding the weakly phased *reduced* PO current [cf. (11.18)–(11.22)]

$$\mathcal{J}^g_{PO}(x,\mathbf{r}',\omega) = J^g_{PO}(x,\mathbf{r}',\omega)\exp\left[ik_1 x\tan\alpha(x)\right] \tag{26}$$

the resulting transmitted field is parameterized in terms of NW-GBs launched from lattice points $(x_{m_2}, h(x_{m_2}))$, $x_{m_2} = m_2 L_2$, into the halfspace $z > h(x)$, analogous to what is done in (15). We obtain (see Fig. 4)

$$G_b(\mathbf{r},\mathbf{r}',\omega) \sim \frac{1}{2}\sum_{|m_2|\le\left(\frac{d}{2L_2}\right)} C^g_{m_2}(\mathbf{r}',\omega)\tilde{\mathcal{B}}^g_{m_2}(\mathbf{r},\omega), \tag{27}$$

$$C^g_{m_2}(\mathbf{r}',\omega) \approx \left(\frac{L_2}{\sqrt{2}}\right)^{\frac{1}{2}} J^g_{PO}(x_{m_2},\mathbf{r}'\omega) \times \exp(ik_1 x_{m_2}\tan\alpha_{m_2}) \tag{28}$$

$$\tilde{\mathcal{B}}^g_{m_2}(\mathbf{r},\omega) \sim ik_0 2^{\frac{5}{4}}\left(\frac{L_2}{8\pi k_0}\right)^{\frac{1}{2}} \frac{\left(\zeta_{m_2} - ib^g_{m_2}\cos\theta^g_{m_2}\right)}{\left(\tilde{R}^g_{m_2}\right)^{\frac{3}{2}}} \times \exp\left\{i\left[k_0\left(\tilde{R}^g_{m_2} + \sqrt{\epsilon_{r1}}x_{m_2}\tan\alpha_{m_2} + ib^g_{m_2}\right) + \frac{\pi}{4}\right]\right\} \tag{29}$$

$$\theta^g_{m_2} = \sin^{-1}\left(\sqrt{\epsilon_{r1}}\sin\alpha_{m_2}\right),\ \alpha_{m_2} = \alpha(x_{m_2}) \tag{30}$$

$$\zeta_{m_2} = -\left(x - x_{m_2}\right)\sin\alpha_{m_2} + \left[z - h(x_{m_2})\right]\cos\alpha_{m_2} \tag{31}$$

$$\tilde{R}^g_{m_2} = \sqrt{\left(x^g_{bm_2}\right)^2 + \left(z^g_{bm_2} - ib^g_{m_2}\right)^2}$$

$$\mathrm{Re}\left(\tilde{R}^g_{m_2}\right) \ge 0 \tag{32}$$

$$\begin{bmatrix} x^g_{bm_2} \\ z^g_{bm_2}\end{bmatrix} = \begin{bmatrix}\cos\gamma^g_{m_2} & -\sin\gamma^g_{m_2}\\ \sin\gamma^g_{m_2} & \cos\gamma^g_{m_2}\end{bmatrix}\begin{bmatrix} x - x_{m_2}\\ z - h(x_{m_2})\end{bmatrix}$$

$$\gamma^g_{m_2} = \theta^g_{m_2} - \alpha_{m_2}, \tag{33}$$

$$b^g_{m_2} = \frac{\left(L_2\cos\alpha_{m_2}\cos\theta^g_{m_2}\right)^2}{\lambda_0}. \tag{34}$$

Note that possible evanescent contributions arising from total reflection are not accounted for in this simple model; in case $\sin\theta^g_{m_2} > 1$, the corresponding GB is simply ignored. Also note that, as in (15), the discretization in (27) is limited to the region $|x| \le d/2$, although now the line-source illumination does not necessarily vanish outside. However, in all numerical simulations presented in Section VI, it was verified that possible truncation-induced (late-time) effects were essentially negligible in the useful observation time-window. Concerning computational burden, the same considerations as in Section IV-B-1 apply.

3) Target-Scattered Field: Using the NW-GB syntheses in Section IV-B- and IV-B2, the FD spectra of the transmitted field E^t and the rough-surface halfspace Green's function G_b are evaluated over the bandwidth of interest, and the TD Born kernel in (14) is computed via FFT [21] (see Section VI-B for details). Note that, in order to accommodate the evanescent spectra in the CSP GB propagators (18) and (19), the analytic signal formulation (one-side Fourier transform) should be used

$$\bar{u}(\mathbf{r},\mathbf{r}',t) = \frac{1}{2\pi c^2}\mathrm{Re}\left[\int_0^\infty \omega^2 E^t(\mathbf{r}',\omega)G_b(\mathbf{r}^r,\mathbf{r}',\omega) \times\exp(-i\omega t)d\omega\right],\quad \mathrm{Im}(t)\le 0. \tag{35}$$

Denoting by $N_{b1} = d/L_1$ and $N_{b2} = d/L_2$ the number of beams used in the GB syntheses (15) and (27), respectively, the computational burden for evaluating the kernel waveform in (35), for fixed frequency and fixed observation and source locations, is thus $\mathcal{O}(N_{b1} + N_{b2})$. As mentioned earlier, a *direct* TD closed-form synthesis could also be obtained in terms of rapidly computable confluent hypergeometric functions, paralleling the procedure in [11, Sec. IV]. However, in order to keep track of the frequency dependence, this would require accounting for the element-by-element interaction between the beams in (15) and those in (27), resulting in a *double* beam summation for each space-time sample with a consequent computational burden $\mathcal{O}(N_{b1}\cdot N_{b2})$, which would be considerably more expensive.

V. Rough Surface Underground Imaging

Based on the linear forward scattering model in (13) and on a number of observations of the scattered field waveforms at the receivers, an inversion scheme can be constructed to retrieve the unknown relative permittivity contrast (object function) $\Delta\epsilon_r$ in the test domain $\mathcal{D}^{(\mathrm{test})}$ to be imaged (Fig. 2). We recall that this problem is inherently ill-posed [22] and that only limited-viewing observations and approximate forward modelings are available, in addition to the unavoidable noise and measurement uncertainty of any practically conceivable implementation. As a consequence, classical linear approaches, such as diffraction tomography (see, e.g., [23], [24]), are difficult to apply, and regularization techniques are needed to restore well-posedness and achieve robust reconstructions. This type of problem is analogous to those typically arising in image processing applications such as object boundary detection and image segmentation [25], so that a whole arsenal of well-established tools is available. In this connection, we have been exploring two popular regularization approaches with *edge-preserving* capabilities, based on different parameterizations of the region under investigation.

A. Pixel-Based Reconstruction: L^p Norm Regularization

One of the simplest reconstruction approaches is based on the parameterization of the test domain to be imaged into a number of adequately small pixels, wherein the object function $\Delta\epsilon_r$ is assumed to be uniform. By discretizing the test domain $\mathcal{D}^{(\text{test})}$ into N pixels centered at $\mathbf{r}'_k, k = 1, \ldots, N$, with area Δs, the linear model in (13) can be discretized accordingly as

$$e^s(\mathbf{r}, t) \approx \sum_{k=1}^{N} \Delta\epsilon_r(\mathbf{r}'_k)\, \bar{u}(\mathbf{r}, \mathbf{r}'_k, t)\, \Delta s. \tag{36}$$

Assuming that the scattered field e^s is sampled at N_r receiver locations $\mathbf{r}^r_i, i = 1, \ldots, N_r$, and N_t time instants $t_{ij}, j = 1, \ldots, N_t$ (Fig. 2), the problem can be cast into matrix form as

$$\underline{y} = \underline{\underline{A}} \cdot \underline{x} + \underline{n} \tag{37}$$

where the *known term* $\underline{y}$ is a column vector containing the $N_r \cdot N_t$ space-time samples of e^s, $\underline{\underline{A}}$ is a $(N_r \cdot N_t) \times N$ matrix containing the space-time discretization of the TD kernel $\bar{u}$ in (14), $\underline{x}$ is a N-element column vector containing the *unknown* object function $\Delta\epsilon_r$ at each pixel, and the *noise* vector $\underline{n}$ accounts for measurement uncertainty and unmodeled effects. Specifically

$$\underline{y} = \begin{bmatrix} \underline{y}_1^T & \cdots & \underline{y}_{N_r}^T \end{bmatrix}^T$$

$$\underline{y}_i^T = \left[e^s(\mathbf{r}^r_i, t_{i1}), \cdots, e^s(\mathbf{r}^r_i, t_{iN_t})\right] \tag{38}$$

$$\underline{\underline{A}} = \begin{bmatrix} \underline{A}_{11} & \cdots & \underline{A}_{1N} \\ \vdots & \ddots & \vdots \\ \underline{A}_{N_r 1} & \cdots & \underline{A}_{N_r N} \end{bmatrix}$$

$$\underline{A}_{ik}^T = \Delta s \left[\bar{u}(\mathbf{r}^r_i, \mathbf{r}'_k, t_{i1}), \cdots, \bar{u}(\mathbf{r}^r_i, \mathbf{r}'_k, t_{iN_t})\right] \tag{39}$$

$$\underline{x} = \left[\Delta\epsilon_r(\mathbf{r}'_1), \cdots, \Delta\epsilon_r(\mathbf{r}'_N)\right]^T \tag{40}$$

with $k = 1, \ldots, N$, $i = 1, \ldots, N_r$, and with ^{T} denoting the transpose. Typical regularization approaches convert this inverse scattering problem into an optimization problem where a cost functional, containing both data and model information from (37) and possible prior information about the object function, is minimized. Among them, total variation (TV) [26] is well-known for its *edge-preserving* capabilities and has found several applications in EM inverse scattering scenarios (see, e.g., [6], [27], [28]). Here, we use a more general approach, based on L^p norm regularization (LNR). The inversion of the linear model in (37) is posed as the minimization of the cost functional [29]

$$J_{LNR}(\underline{x}) = \|\underline{y} - \underline{\underline{A}} \cdot \underline{x}\|_2^2 + \beta_1 \|\underline{\underline{D_\nu}} \cdot \underline{x}\|_p^p + \beta_2 \|K(\underline{x})\|_2^2 \tag{41}$$

where $\|\ \|_2$ is the standard Euclidean (L^2) norm and $\|\ \|_p (0 < p \leq 2)$ is an L^p norm [29]. In (41), the first term penalizes lack of data fidelity, while the other terms introduce some loose a priori knowledge about the object geometry, with β_1 and β_2 denoting regularization parameters. In particular, the second term highlights the expected piecewise smoothness in the reconstructed object function by penalizing the L^p norm of a spatial gradient operator $\underline{\underline{D_\nu}}$. In our implementation we chose [6], [30]

$$\|\underline{\underline{D_\nu}} \cdot \underline{x}\|_p^p \equiv \sum_{k=1}^{N} \left\{ \nu [\underline{\underline{D_x}} \cdot \underline{x}]_k^2 + (2-\nu) [\underline{\underline{D_z}} \cdot \underline{x}]_k^2 \right\}^{\frac{p}{2}} \tag{42}$$

where $\underline{\underline{D_x}}$ and $\underline{\underline{D_z}}$ denote standard first-order finite-difference operators in the horizontal and vertical direction, respectively, and the parameter ν controls the orientation preference of the smoothness regularization ($\nu = 1$ yields no orientation preference) [30]. As will be shown, a regularization with orientation preference may give better results, in view of the limited-viewing configuration of the problem, which gives rise to different resolutions achievable in the horizontal and vertical directions. The formulation in (42) reduces to Tikhonov-like regularization [31] for $p = 2$, and to TV-like regularization [26] for $p = 1$. As compared with the L^2 norm in the standard Tikhonov regularization [31], L^p norms with $0 < p \leq 1$ on the spatial gradient term in (42) penalize *large* jumps less, thus allowing sharper edges to form in the reconstructed object function and yielding visually better (less blurred) reconstructions.

The last term in (41) is related to possible prior information about the object function sign. Assuming, for instance, a *negative* value for $\Delta\epsilon_r$ in the target region, the L^2 norm of the operator K penalizes *positive* values (or viceversa) of the reconstructed object function

$$[K(\underline{x})]_k = \begin{cases} x_k, & x_k > 0, \\ 0, & x_k \leq 0. \end{cases} \tag{43}$$

In our implementation, the cost functional in (41) is minimized via an iterative procedure based on half-quadratic approximations (see [26] for details). The proper choice of the regularization parameters β_1 and β_2 in (41) is an important issue, and several strategies have been proposed (see, e.g., [32]), but this is not the focus here. Our choice of the regularization parameters was done by trial and error.

B. Object-Based Reconstruction: Curve Evolution

Object-based techniques have been widely investigated in image processing, with many important applications in problems like object boundary detection and image segmentation [25]. The basic idea underlying these approaches is to exploit parametric or semi-parametric deformable shape models for the object function which incorporate possible a priori information about the target geometry. Prominent among them are *curve evolution* (CE) techniques (see, e.g., [33], [34]) where a *gradient flow* is designed which attracts initial closed curves to the target boundary. Applications of such approaches to EM inverse scattering problems have been proposed in [35]–[37]. In particular, in [37], a CE approach is applied to UWB GPR underground imaging of shallowly-buried low-contrast plastic targets in the presence of a *flat* air-ground interface. This approach is applied here to the more challenging problem of a *rough* air-ground interface. The algorithm in [37] is briefly reviewed. Assuming a scenario with a *single* homogeneous target occupying the region $\mathcal{D}$ (Fig. 2) bounded by a continuous curve $\vec{C}$, the unknown object function can be expressed as

$$\Delta\epsilon_r(\mathbf{r}) = \overline{\Delta\epsilon_r} \Pi_{\mathcal{D}}(\mathbf{r}) \tag{44}$$

where $\overline{\Delta\epsilon_r} = \epsilon_{r2} - \epsilon_{r1}$, and $\Pi_{\mathcal{D}}$ is the characteristic function of the target region $\mathcal{D}$

$$\Pi_{\mathcal{D}}(\mathbf{r}) = \begin{cases} 1, & \mathbf{r} \in \mathcal{D} \\ 0, & \mathbf{r} \notin \mathcal{D}. \end{cases} \tag{45}$$

The more general case of multiple connected or unconnected components is addressed in [37]. The parameterization in (44) contains *implicit* regularization, since the reconstructed object must be homogeneous. In this connection, the reconstruction task consists in estimating the target contour $\vec{C}$ and the permittivity contrast $\overline{\Delta\epsilon_r}$. Using (44), the linear model in (13) can be rewritten as

$$e^s(\mathbf{r}, t) \approx \overline{\Delta\epsilon_r} \int\int_{\mathcal{D}} \bar{u}(\mathbf{r}, \mathbf{r}', t) d\mathbf{r}'. \tag{46}$$

We assume, as in Section V-A, that a set of $N_r \cdot N_t$ samples of the scattered field is collected at N_r receiver locations $\mathbf{r}_i^r, i = 1, \ldots, N_r$, at N_t time instants $t_{ij}, j = 1, \ldots, N_t$ (Fig. 2). The problem of estimating target boundary and permittivity contrast is posed again as an optimization problem involving minimization of the following quadratic functional [37]

$$J_{CE}(\vec{C}, \overline{\Delta\epsilon_r}) = \frac{1}{2} \sum_{i=1}^{N_r} \sum_{j=1}^{N_t} \left(e_{ij}^s - \overline{\Delta\epsilon_r} U_{ij}\right)^2 + \beta \int_{\vec{C}} d\ell. \tag{47}$$

As in (41), the cost functional in (47) contains a data fidelity term, where $e_{ij}^s = e^s(\mathbf{r}_i^r, t_{ij})$ and

$$U_{ij} = \int\int_{\mathcal{D}} \bar{u}\left(\mathbf{r}_i^r, \mathbf{r}', t_{ij}\right) d\mathbf{r}'. \tag{48}$$

The second term serves as regularization by penalizing the arclength of the estimated curve, with the choice of the regularization parameter β in (47) affecting its smoothness. Again, in our implementation, β is empirically selected by trial and error, taking into account prior expectations about target geometry (e.g., convexity).

To minimize the cost functional in (47), we use a CE approach to design a gradient flow that attracts an initial closed curve to the boundary of the target region $\mathcal{D}$. Given a family of smooth curves $\vec{C}(\tau)$ parameterized by τ, we search for the curve in this family and the contrast value $\overline{\Delta\epsilon_r}$ that minimize the cost functional in (47). For a given curve $\vec{C}(\tau)$, the contrast $\overline{\Delta\epsilon_r}$ must satisfy the following equation [37]

$$\frac{\partial J_{CE}(\tau, \overline{\Delta\epsilon_r})}{\partial \overline{\Delta\epsilon_r}} = -\sum_{i=1}^{N_r} \sum_{j=1}^{N_t} \left[e_{ij}^s - \overline{\Delta\epsilon_r} U_{ij}(\tau)\right] U_{ij}(\tau) = 0. \tag{49}$$

Moreover, it can be shown (see [37] for details) that the gradient direction of J_{CE} with respect to the curve $\vec{C}(\tau)$ is given by

$$\nabla_\tau J_{CE}(\tau, \overline{\Delta\epsilon_r}) = -\sum_{i=1}^{N_r} \sum_{j=1}^{N_t} \left[e_{ij}^s - \overline{\Delta\epsilon_r} U_{ij}(\tau)\right] \overline{\Delta\epsilon_r} \bar{u}_{ij}\left(\mathbf{r}_c'\right) \hat{\mathbf{n}}_c + \beta \kappa_c \hat{\mathbf{n}}_c \tag{50}$$

where $\bar{u}_{ij}(\mathbf{r}_c') = \bar{u}(\mathbf{r}_i^r, \mathbf{r}_c', t_{ij})$, $\mathbf{r}_c'$ denotes points on the curve $\vec{C}(\tau)$, and $\hat{\mathbf{n}}_c$ and κ_c indicate the outward normal and the signed curvature of the curve at $\mathbf{r}_c'$, respectively [37]. To minimize the cost functional in (47), the curve $\vec{C}(\tau)$ is evolved along the direction of steepest descent, i.e., along the negative gradient of J_{CE} with respect to $\vec{C}(\tau)$

$$\begin{aligned} \frac{d\vec{C}(\tau)}{d\tau} &= -\nabla_\tau J_{CE}(\tau, \overline{\Delta\epsilon_r}) \\ &= \sum_{i=1}^{N_r} \sum_{j=1}^{N_t} \left[e_{ij}^s - \overline{\Delta\epsilon_r} U_{ij}(\tau)\right] \\ &\quad \times \overline{\Delta\epsilon_r} \bar{u}_{ij}\left(\mathbf{r}_c'\right) \hat{\mathbf{n}}_c - \beta \kappa_c \hat{\mathbf{n}}_c \end{aligned} \tag{51}$$

where, for each τ, the optimal value of the contrast $\overline{\Delta\epsilon_r}$ is given by (49). For numerical implementation, the evolution in (51) is discretized in τ and stepped forward, alternatively updating the curve $\vec{C}(\tau)$ and the contrast $\overline{\Delta\epsilon_r}$ (via (49)). In our implementation, we use the level set method [38], [39] which yields a numerically efficient and stable evolution (see [37]).

As compared with pixel-based reconstruction techniques, object-based approaches like CE offer several computational advantages. First is the natural incorporation of a priori information about target constitutive and geometric features, such as homogeneity and shape smoothness. This allows use of efficient parametric models to describe target shape and permittivity contrast, with consequent *implicit* regularization which mitigates the ill-posedness of the problem and possibly reduces the data size required. Furthermore, it focuses on the key features of the target, which are estimated *directly* rather than extracted via postprocessing of a pixel-based image. Finally, the evolution in (51) depends mostly on *local* properties, and the estimation of the contrast value in (49) is computationally inexpensive, resulting in an overall computational burden that tends to be lower than those of standard pixel-based approaches like LNR.

VI. Numerical Results

A. Reference Solution

The backscattered field data used as observations are simulated via a full-wave solution of the forward scattering problem. As in [11], this reference solution is based on the time-harmonic multifilament current method in [40], adapted to moderately rough interfaces. Specifically, the frequency domain (FD) spectrum of the field is evaluated at 100 different frequencies within the pulse bandwidth, without resorting to the plane wave approximation in (1) for the incident field, and with use of the full dispersive permittivity model for the soil. The sampled spectrum is first smoothed through local Padé-approximation [21] and then transformed via standard inverse fast Fourier transform (FFT) routines [21] to obtain the desired TD solution. In our numerical simulation we used a 1024-point FFT; the required TD samples were obtained by linear interpolation of the returned time series.

B. Gaussian Beam Algorithm Parameters

The Born TD kernel $\bar{u}$ in (35), needed for computing the data fidelity term in both LNR and CE cost functionals, is first synthesized in the FD via NW-GB superposition [cf. (15) and (27)] and subsequently transformed to the TD via a 512-point FFT. In this case, the spectrum is sampled at 50 frequencies within the

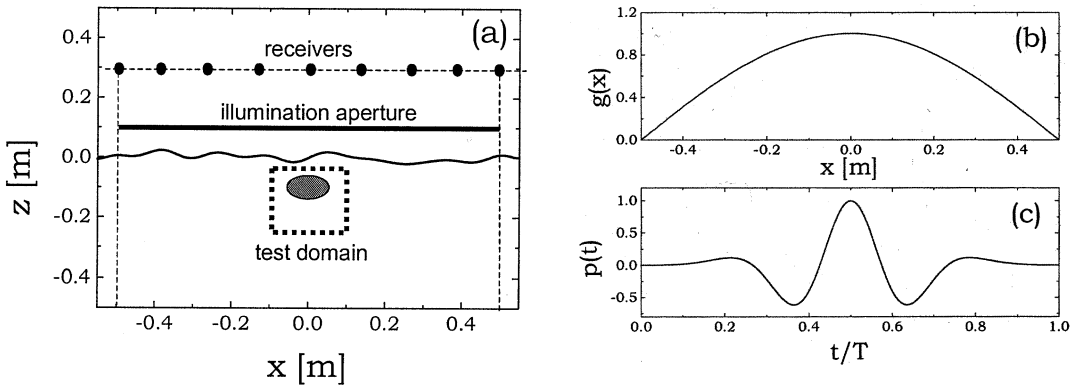

Fig. 5. Simulation geometry and parameters (cf. Fig. 2). (a) An elliptic (10 cm × 6 cm) dielectric mine-like target with $\epsilon_{r2} = 3.5$ and $\sigma_2 = 0$ is buried with center at 10 cm below the nominal ground ($z = 0$). The rough surface profile realization was randomly generated so as to simulate typical moderate roughness (maximum-to-minimum height ∼4 cm, maximum slope ∼ 32°) for a class of realistic soils ($\epsilon_{r1} = 4$, $\sigma_1 = 0.01$ S/m). A 20 cm × 20 cm test domain surrounding the target (with top side at 5 cm below nominal ground) is to be imaged. The reflected field is sampled at $N_r = 11$ receivers located at $z^r = 0.3$ m and $x_i^r = -0.5$ m, -0.4 m, …, 0.5 m. (b) Incident field tapering $g(x) = \cos(\pi x/d)$. Parameters: $d = 1$ m, $\theta_A = 0$, $x_A = 0$, $z_A = 0.1$ m. (c) Fourth-order Rayleigh pulsed excitation $p(t)$ ($cT = 0.4\ d$, i.e., $T \sim 1.3$ ns).

pulse bandwidth. All other needed frequency samples, as well as the output time waveform, are obtained via linear interpolation. The GB spacings L_1 and L_2 in (15) and (27), respectively, are chosen as half a (ambient) wavelength, i.e., $L_1 = |\lambda_1|/2$, $L_2 = \lambda_0/2$. This configuration was arrived at using a *pragmatic* stability criterion based on the (in)sensitivity of the outcome to further decreases of the GB spacing (i.e., increases in the number of GBs). To further improve computational efficiency, for a fixed observation point, one can rewrite the CSP GB propagators in (18) and (29) [see, e.g., (11.52)–(11.54)] to isolate frequency-independent parts that need to be computed only once.

C. Simulation Parameters

The numerical simulations that follow are based on the configuration and parameters described in Fig. 5. In this scenario (Fig. (5a)), although no specific data model is used for soil, target and roughness, geometric and constitutive parameters were adjusted so as to be consistent with typical moderate roughness (maximum-to-minimum height ∼4 cm, maximum slope ∼ 32°), slightly lossy soil characteristics [41] ($\epsilon_{r1} = 4$, $\sigma_1 = 0.01$ S/m), and shallowly-buried plastic mine-like targets (10 cm × 6 cm ellipse with $\epsilon_{r2} = 3.5$ and $\sigma_2 = 0$, and with center at 10 cm below nominal ground). The roughness profile was randomly generated via the quartic spline model in [13, Sec. IV]. The illumination field in (1) was chosen as a vertically incident fourth-order Rayleigh UWB pulse with $T = 1.3$ ns [Fig. 5(c)] and cosine tapering [Fig. 5(b)]. This pulse length was found by trial and error to provide a good tradeoff between the contrasting high-frequency requirements for good resolution (for both surface estimation and target localization) and low-frequency requirements for adequate soil penetration. Such UWB pulses typically work well for shallow burial depths and slightly lossy soils, as in our example, but may be not suitable for larger burial depths and/or soil losses.

The test domain to be imaged consists of a 20 cm × 20 cm domain surrounding the target, with top side at 5 cm below nominal ground. The backscattered field observation data needed for inversion are collected at $N_r = 11$ receivers at $z^r = 0.3$ m and $x_i^r = -0.5$ m, -0.4 m, …, 0.5 m. Note that the relatively low permittivity contrast in this example ($|\Delta\epsilon_r|/\epsilon_{r1} = 0.125$), which justifies the Born approximation in (13), renders the test particularly challenging in view of the weak target scattering as compared with the interface-generated clutter. The burial depth was chosen so as to avoid the relatively clean case where ground-scattered and target-scattered signals are well time-resolved (see Section VI-D).

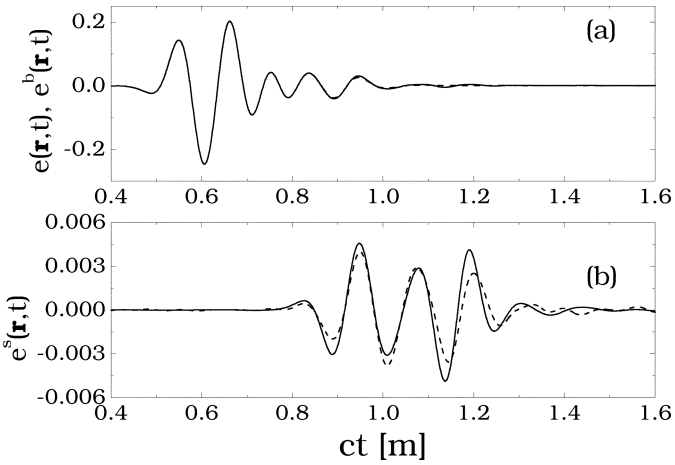

Fig. 6. Parameters as in Fig. 5. Field observed at receiver #8 ($x_8^r = 0.3$ m, $z^r = 0.3$ m) (a) — Total field e (reference solution); - - - Background field e^b (reference solution). Both are coincident on this drawing. (b) Target-scattered field $e^s = e - e^b$. — Reference solution - - - Beam-Born approximation in (13) (parameters as in Section VI-B).

D. Reconstruction Examples

1) Parameterization Issues: Before testing the various underground imaging strategies, it is useful to look at the scattered waveforms at the receivers, in order to identify the various contributions and to check the accuracy of the Born-GB forward scattering model. Fig. 6(a) shows the comparison between the total field e (soil+target) and the background field e^b (soil only) waveforms at a fixed receiver location, computed via the full-wave technique described in Section VI-A. The two waveforms are practically indistinguishable in the plot scale. Their

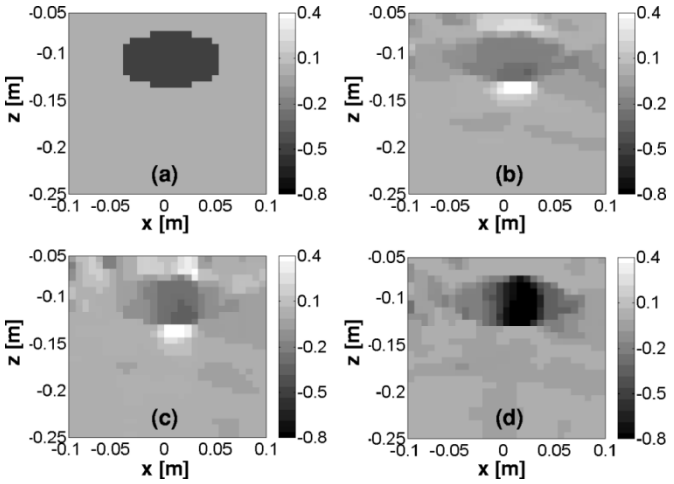

Fig. 7. Parameters as in Fig. 5. (a) Ground truth ($\Delta\epsilon_r$ reference configuration). (b) TVL ($p = 1$) reconstruction ($\beta_1 = 1.6 \cdot 10^{-6}$, $\nu = 1$, $\beta_2 = 0$; $\Delta e_t = -19$ dB, $\Delta e_b = -35$ dB). (c) TVL reconstruction with directional preference ($\beta_1 = 4.6 \cdot 10^{-6}$, $\nu = 0.1$, $\beta_2 = 0$; $\Delta e_t = -19$ dB, $\Delta e_b = -35$ dB). (d) TVL reconstruction with directional preference and positivity penalty ($\beta_1 = 3.4 \cdot 10^{-6}$, $\nu = 0.1$, $\beta_2 = 2 \cdot 10^{-3}$; $\Delta e_t = -22$ dB, $\Delta e_b = -37$ dB). The exact air-soil interface profile is used in the forward scattering model.

difference (the target contribution e^s) is displayed in Fig. 6(b) and is compared with the Born-GB synthesis described in Section VI-B. Reasonably good agreement is observed. Looking at the different scales in the two plots, it is noted that background field removal is crucial for achieving reasonable signal-to-noise ratio in the inverse scattering procedure. For rough interfaces and shallowly-buried targets, as in this example, this cannot usually be accomplished by mere time-windowing of the data since ground-scattered and target-scattered signals are *not* well time-resolved. In this connection, the availability of rough interface profile estimations (and hence background field predictions) is of great importance.

Another important issue is the choice of the actual number of unknowns in the object parameterization. This requires tradeoff between resolution, robustness and computational burden. Aside from computational considerations, it is understood that beyond a critical level, related to the *essential* dimension of the available information, any attempt at further refinement in the object discretization will increase the sensitivity to noise, *without* actually improving the resolution. The essential information entailed in the forward scattering model can be estimated roughly, for instance, via singular value decomposition [21] of the (discretized) scattering kernel in (14), whereas the prior information introduced with the various regularization techniques cannot be easily quantified. We did not attempt to address *optimal* strategies for object discretization and data acquisition. The data and unknown configurations used in the examples, though not necessarily optimal, were found to provide a reasonable tradeoff between the above contrasting requirements. In particular, to account for possible redundancy in the observed data, in all examples below we retain a data-to-unknown ratio $\sim$3.

For pixel-based reconstruction with L^p norm regularization (LNR), the test domain to be imaged was discretized into 30 $\times$ 30 square pixels (900 unknowns), and we used $N_t = 300$ time samples of the *late-time* response (causally related to the test domain) at each of the $N_r = 11$ receivers in Fig. 5. The observation vector $\underline{y}$ in (38) was obtained by subtracting the PO-PB-computed background field e^b (see [11]) from the full-wave-computed total field e at each receiver; the (3300 $\times$ 900) data matrix $\underline{\underline{A}}$ in (39) was computed via the Born-GB algorithm (see Section VI-B). In all examples below, the various regularization parameters were selected pragmatically via trial and error, and the results reported correspond to the *best* reconstruction obtained. Reconstruction results, however, were found to be relatively insensitive to variation of these parameters within a calibrated range.

We now move on to presenting various examples of underground imaging results.

2) Perfectly Known Roughness Profile and Soil Parameters, and Noiseless Data: We start with the simplest, though somewhat unrealistic, case of perfectly known roughness profile and soil parameters, and noiseless observation data, on which we test the various reconstruction techniques presented so far. A number of representative pixel-based reconstruction examples are shown in Fig. 7. Specifically, the true object function (ground truth) is shown in Fig. 7(a), while Fig. 7(b)–(d) display a number of LNR reconstructions with $p = 1$, i.e., total-variation-like (TVL), with various combinations of the regularization parameters, namely, *i*) gradient penalty without directional preference, i.e., $\beta_2 = 0$ in (41) and $\nu = 1$ in (42) [Fig. 7(b)]; *ii*) gradient penalty with directional preference, i.e., $\beta_2 = 0$ and $\nu = 0.1$ [Fig. 7(c)]; and *iii*) gradient penalty with directional preference and "positivity penalty," i.e., $\beta_2 > 0$ and $\nu = 0.1$ [Fig. 7(d)]. It is observed that all TVL images, though not yielding highly accurate point-wise reconstructions, provide reasonably accurate target localization. Note that the limited-viewing geometry (vertical illumination) renders the problem *more ill-posed* in the horizontal direction, thus resulting in higher vertical than horizontal resolution in all cases. In this connection, gradient penalty with *directional* preference turns out to be more effective since the data fidelity term is less sensitive to horizontal than vertical blurring. If the gradient penalty is equally imposed on both directions [as in Fig. 7(b)], it is possible that the vertical direction is under-regularized while the horizontal direction is over-regularized. Therefore, a gradient penalty with $\nu < 1$ [smaller in the horizontal direction, as in Fig. 7(c)] may help in compensating for this imbalance, and yield visually better reconstructions. Looking at Fig. 7(d), it is realized that prior knowledge of the object function sign, and consequent positivity (or negativity) penalty in the cost functional, may further improve the reconstruction.

For more *quantitative* accuracy assessments, we introduced two simple rms error metrics in both target and background regions

$$\Delta e_t \equiv \frac{\sum_{\mathbf{r}'_k \in \mathcal{D}} \left[\epsilon_{r2} - \epsilon_{r2}^{(est)}(\mathbf{r}'_k)\right]^2}{N_2 \epsilon_{r2}^2}$$

$$\Delta e_b \equiv \frac{\sum_{\mathbf{r}'_k \notin \mathcal{D}} \left[\epsilon_{r1} - \epsilon_{r1}^{(est)}(\mathbf{r}'_k)\right]^2}{N_1 \epsilon_{r1}^2} \qquad (52)$$

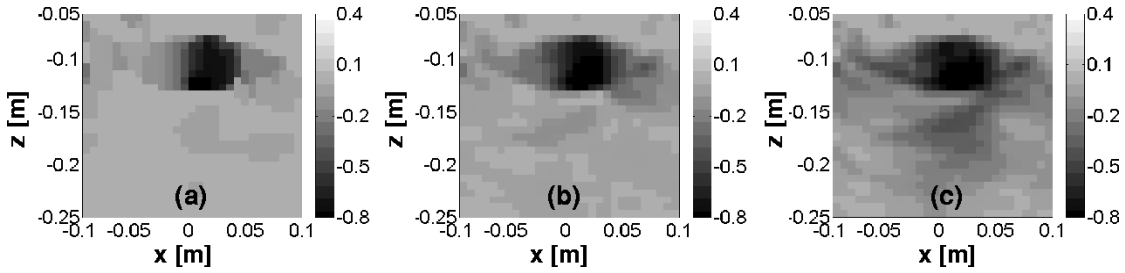

Fig. 8. As in Fig. 7, but using LNR with $p \neq 1$, directional preference and positivity penalty ($\beta_1 = 3.4 \cdot 10^{-6}$, $\nu = 0.1$, $\beta_2 = 2 \cdot 10^{-3}$). (a) $p = 0.5$ ($\Delta e_t = -22$ dB, $\Delta e_b = -40$ dB). (b) $p = 1.5$ ($\Delta e_t = -23$ dB, $\Delta e_b = -33$ dB). (c) $p = 2$ (Tikhonov, $\Delta e_t = -24$ dB, $\Delta e_b = -27$ dB). The case $p = 1$ (TVL) is displayed in Fig. (7d).

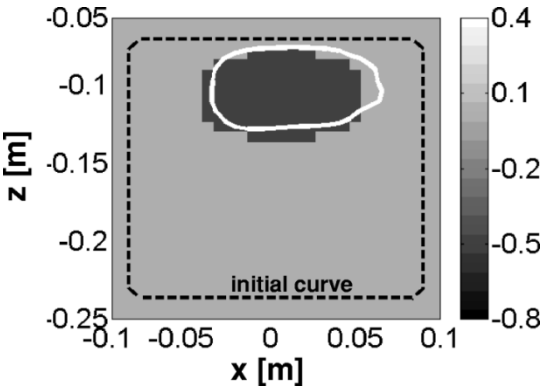

Fig. 9. Parameters as in Fig. 5. Curve evolution reconstruction (white curve) is superposed on ground truth. Curve initial conditions are displayed by dashed lines. Evolution parameters: 150 steps with $\beta = 3.5 \cdot 10^{-5}$ plus 620 steps with $\beta = 0.3 \cdot 10^{-5}$. The estimated target relative permittivity is $\epsilon_{r2} = 3.52$ (0.6% error). The rms errors in target and background regions are $\Delta e_t = -25$ dB and $\Delta e_b = -37$ dB, respectively. The exact air-soil interface profile is used in the forward scattering model.

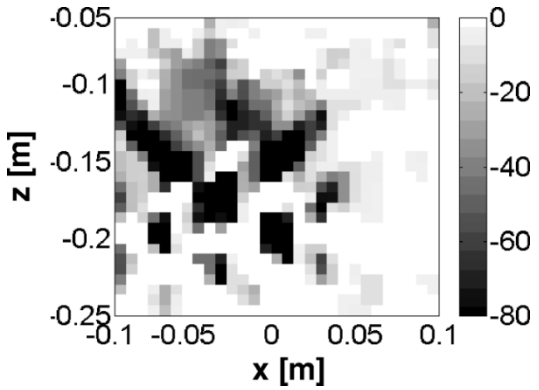

Fig. 10. As in Fig. 6(d) ($\beta_1 = 3.4 \cdot 10^{-6}$, $\nu = 0.1$, $\beta_2 = 2 \cdot 10^{-3}$), but assuming a flat interface at $z = 0$ in the forward scattering model ($\Delta e_t = 27$ dB, $\Delta e_b = 28$ dB).

where $\epsilon_{r1}^{(est)}$ and $\epsilon_{r2}^{(est)}$ denote the estimated relative permittivity in the background and target regions, respectively, while N_1 and N_2 indicate the corresponding number of pixels. These errors are specified (in dB) in the figure captions. It is observed from Fig. 7 that gradient penalty with directional preference coupled with positivity penalty [Fig. 7(d)] yields the smallest errors ($\Delta e_t = -22$ dB, $\Delta e_b = -37$ dB).

Reconstruction examples for $p = 0.5$, 1.5 and 2 (with directional preference and positivity penalty) are shown in Fig. 8. By comparing these reconstructions, together with that for the corresponding TVL (i.e., $p = 1$) in Fig. 7(d), one notes progressive blurring toward the Tikhonov-like [$p = 2$, Fig. 8(c)] reconstruction. However, LNR with $p < 1$ [e.g., $p = 0.5$ in Fig. 8(a)] was found not to yield significant improvement as compared with TVL, and the corresponding results are omitted henceforth.

Fig. 9 shows a reconstruction obtained via CE, which provides good estimation of both target boundary and permittivity (only 0.6% error in ϵ_{r2}). The reconstruction looks visually better than the corresponding TVL one in Fig. 7(d), as also witnessed by the smaller rms errors, $\Delta e_t = -25$ dB, $\Delta e_b = -39$ dB, computed from (52) with the same pixelization used for LNR. Again, due to the limited-viewing configuration, localization is more accurate vertically than horizontally. For this reconstruction, a reduced data set was used, with only 6 receivers (#1, 3, 5, 7, 9, and 11, in Fig. 5) and 100 time samples each, taking advantage of the more compact object parameterization entailed in CE as compared with pixel-based reconstruction techniques.

3) Imperfectly Known Roughness Profile and Soil Parameters, and Noisy Data: We now explore more realistic configurations by removing the assumption of perfect knowledge of the air-soil rough interface as well as soil parameters and observation data. First, to highlight the effect of the air-ground interface roughness, so far assumed to be perfectly known, we show in Fig. 10 a TVL reconstruction obtained by *erroneously* assuming a flat air-ground interface at $z = 0$ in the forward scattering model. Image deterioration, mainly due to poor background field removal, is dramatic and renders the reconstruction practically meaningless. For this configuration, CE likewise gave meaningless results, exhibiting strong sensitivity to initial conditions and regularization parameters. Results can be improved via statistical processing, as shown in [6], but will not become comparable to those in Figs. 7–9.

Now, we use the algorithm in [13] (see also Section III) to generate estimations of the rough interface to be used in the subsequent underground imaging problem. We also investigate the effect of measurement uncertainty in the observation data as well as soil parameters. Fig. 11 shows the rough interface reconstructions obtained with two different data configurations: *i*) corruption of the observation data with an additive uniform noise ($\pm 10\%$ in amplitude) that accounts for measurement uncertainty and unmodeled effects (e.g., finer-scale roughness scattering), and *ii*) assumption of a -5% error in ϵ_{r1} and σ_1 in the forward scattering model. For these reconstructions, as discussed in [13], we used $N_t = 50$ time samples of the *early-time*

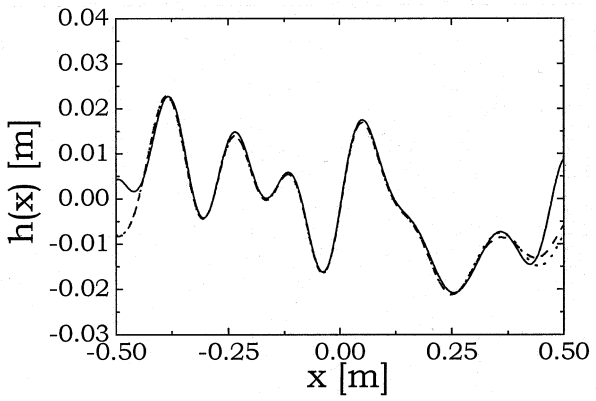

Fig. 11. Parameters as in Fig. 5. Rough surface profile reconstruction via early-time response processing (cf. Section III and [13]). The early-time field at the receivers is sampled at $N_t = 50$ time instants with the observation windows chosen so as to roughly gate out causal scattering contributions from regions deeper than $\sim$8 cm below nominal ground. — Actual profile; - - - Reconstruction with observation data corrupted by a $\pm 10\%$ additive uniform noise; $\cdots\cdots$ Reconstruction with -5% error in ϵ_{r1} and σ_1.

response at each of the 11 receivers in Fig. 5; the observation time-windows were chosen so as to roughly gate out scattering contributions from possible regions deeper than $\sim$8 cm below nominal ground ($z = 0$), thus minimizing possible bias due to target scattering. Interface estimates are reasonably accurate (see Fig. 11), apart from the weakly-illuminated edge regions, as also observed in [13]. Although the $\sim$8 cm time window is not perfectly consistent with the early-time constraint for interface-target isolation in the model of Fig. 5, the interface profile reconstructions obtained in the presence of the target appear to be remarkably insensitive to this pollution. We recall that these model configurations are particularly challenging because the -5% relative permittivity mismatch in the second example is on the same order as the actual contrast $\Delta\epsilon_r = -0.5$ to be estimated. The corresponding TVL and CE target reconstructions are shown in Fig. 12, where a slightly narrower illumination ($d = 0.8$ m) is used in order to de-emphasize the effect of the poorly estimated side regions in Fig. 11. Specifically, Fig. 12(a) and (b) show TLV and CE reconstructions, respectively, for the case of noisy data (with perfectly known soil parameters), whereas Fig. 12(c) and (d) show the corresponding results for the case of imperfectly known soil parameters (with noiseless data). In these examples, the corresponding estimated air-soil interface profiles in Fig. 11 are used in the forward scattering model. As seen from Figs. 12(a) and (b), reconstructions turn out to be robust with respect to noise in the observation data. In particular, CE still yields good target localization and permittivity estimation (1.7% error in ϵ_{r2}; $\Delta e_t = -23$ dB, $\Delta e_b = -39$ dB). For the TVL reconstruction, rms errors ($\Delta e_t = -21$ dB, $\Delta e_b = -31$ dB) are still comparable to those obtained in the *ideal* case [Fig. 7(d)]. For the more challenging soil-parameter-mismatch test in Fig. 12(c) and (d), although the target shape is not as accurately captured as before, localization and permittivity estimation (1.7% error in ϵ_{r2}, and $\Delta e_t = -26$ dB, $\Delta e_b = -25$ dB with CE; $\Delta e_t = -15$ dB, $\Delta e_b = -22$ dB with TVL) are still acceptable for classification purposes. Since the assumed mismatch in the soil parameters

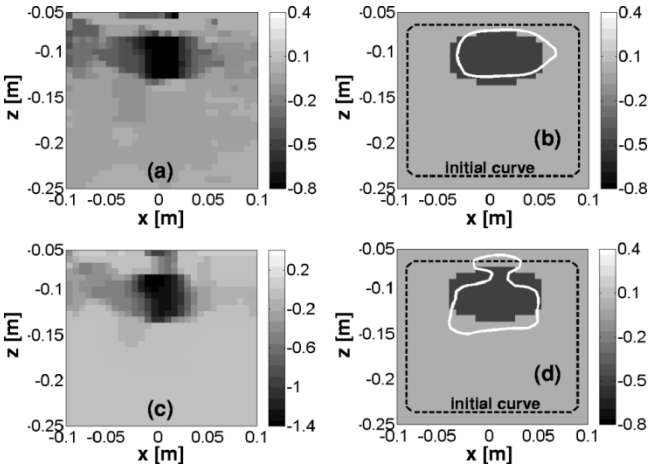

Fig. 12. Parameters as in Fig. 5, but with $d = 0.8$. Reconstruction examples with corrupted data via TVL regularization and CE. (a) TVL reconstruction with field data observations corrupted by $\pm 10\%$ additive uniform noise ($\beta_1 = 3.4 \cdot 10^{-6}$, $\nu = 0.1$, $\beta_2 = 2 \cdot 10^{-3}$, $\Delta e_t = -21$ dB, $\Delta e_b = -31$ dB). (b) As in Fig. (12a), but CE reconstruction (white curve) superposed on ground truth (150 steps with $\beta = 3.5 \cdot 10^{-5}$ plus 627 steps with $\beta = 0.3 \cdot 10^{-5}$; estimated target permittivity: $\epsilon_{r2} = 3.56$, i.e., 1.7% error; $\Delta e_t = -23$ dB, $\Delta e_b = -39$ dB). (c) TVL reconstruction with -5% error in ϵ_{r1} and σ_1 ($\beta_1 = 3.4 \cdot 10^{-6}$, $\nu = 0.1$, $\beta_2 = 2 \cdot 10^{-3}$, $\Delta e_t = -15$ dB, $\Delta e_b = -22$ dB). (d) As in Fig. (12c), but CE reconstruction (white curve) superposed on ground truth (150 steps with $\beta = 3.5 \cdot 10^{-5}$ plus 640 steps with $\beta = 0.21 \cdot 10^{-5}$; estimated target permittivity: $\epsilon_{r2} = 3.56$, i.e., 1.7% error; $\Delta e_t = -26$ dB, $\Delta e_b = -25$ dB). The *estimated* air-soil interface profiles in Fig. 11 are used in the forward scattering model.

TABLE I
CALIBRATED RANGE OF APPLICABILITY OF THE IMPLEMENTED APPROACH FOR THE EXCITATION SPECIFIED IN FIG. 5(b) AND(c). $\alpha_{\max}$ AND $\bar{r}_c$ INDICATE THE INTERFACE PROFILE MAXIMUM SLOPE AND AVERAGE RADIUS OF CURVATURE, RESPECTIVELY; Ω_0 INDICATES THE EFFECTIVE BANDWIDTH OF THE EXCITATION PULSE $p(t)$

Parameter	Calibrated range	Specific limiting factors (if any)
Rough surface parameters	$\alpha_{max} < 40^o$ $\bar{r}_c > 20$cm	PO approximation; imperfect interface reconstruction
Target depth (top side)	> 4cm	PO, far-field approximations; difficult interface-target isolation for strong residual clutter
	< 15cm	Signal attenuation
Target contrast	$\Delta\epsilon_r/\epsilon_{r1} > 0.1$	Low target visibility
	$\Delta\epsilon_r/\epsilon_{r1} < 0.25$	Born approximation
Soil parameters	$\sigma_1 < 0.05\Omega_0\epsilon_0\epsilon_{r1}$	Slight loss assumption
Noise (uniform)	up to $\pm 10\%$	
Uncertainty in ϵ_{r1}, σ_1	up to $\pm 5\%$	

reduces the *effective* visibility of the (already low-contrast) target, this mismatch renders the background field removal more critical. Evidently, for such low-contrast target scattering scenarios, *stronger* uncertainty in the soil parameters may render the target practically invisible.

4) Calibration and Performance Assessment: The calibrated range of applicability of the algorithm, obtained through a set of 36 numerical experiments with various roughness profile realizations and soil/target parameters, and for the excitation specified in Fig. 5(b) and (c), is summarized in

TABLE II
SUMMARY OF COMPUTATIONAL FEATURES. COMPUTING TIMES SHOWN ARE REGARDED AS AVERAGE FOR A REFERENCE IMPLEMENTATION ON A 700 MHz PC

Task	Implementation	Computing time [secs.]		Memory [Mbytes]	
		LNR	CE	LNR	CE
Interface estimation	C++	55		-	-
Background field removal	C++	1	0.4	-	-
Data matrix filling up	C++	120	62	-	-
Target imaging	Matlab™	185	127	22.6	4.1

Table I. In all simulations, the *estimated* air-soil interface profiles are used in the forward scattering model. As can be observed from Table I, some of the limitations are related to various utilized field-based approximations (e.g., PO, paraxial far field GB asymptotics, etc.), while others are related to the model-based adaptive data-processing, which breaks down when the interface roughness profile is poorly estimated and/or the interface-target separation is not large enough to allow the sequential (early/late-time) imaging. While the various constraints in our synthetic model legitimize only appropriately tuned narrow windows of applicability, the corresponding physical parameters are reasonable for actual GPR scenarios. As noted earlier, we were encouraged by the observed insensitivity in our end-to-end synthetic model to weak violations of the cited constraints. As with any model-based synthetic algorithm, its performance in the presence of *real* data remains to be explored.

E. Computational Aspects

The overall computational features of the proposed approach are detailed in Table II for each of the separate tasks required, with specific reference to a 700 MHz PC reference implementation. The computational burdens of the first four tasks are strongly tied to those of the NW-GB forward solvers in [11] and Sections IV-B and VI-B. In this connection, the reported (average) computing times were found to be about four times and two times smaller than those achievable with standard PO implementations and with the quasi-real ray tracing in [10], respectively. Meaningful comparisons with full-wave forward solvers are not straightforward since computational features may be strongly implementation-dependent. Based on our forward scattering benchmark simulations, rough estimates of full-wave computing times for the air-soil interface reconstruction and for building up the forward model data matrix have been on the order of eight and four hours, respectively.

As seen from Table II, the only memory-demanding tasks are those involving the manipulation of the LNR data matrix $\underline{\underline{A}}$ in (41) and a similar (but smaller) data matrix used in the CE (51) via the level set method.

Overall, CE tends to be computationally cheaper than LNR. Although the numerical codes are not fully optimized, overall computing times are on the order of a few minutes, thus leaving room for optimism that extensions of the algorithmic approach to more realistic 3-D scenarios will remain computationally affordable for real-world applications.

VII. CONCLUSION

An adaptive approach for underground imaging via ultra-wide-band GPR in the presence of a specified moderately rough air-soil interface has been presented. The proposed approach is based on short-pulse Gabor-based narrow-waisted quasi-ray Gaussian beam algorithms as fast forward scattering models, through which the coarse-scale deterministic features of the air-ground interface are first estimated from early-time data and subsequently exploited to compensate for background clutter and distortion in the late-time target-interrogating signal. Preliminary 2-D numerical experiments, carried out so far with synthetic data and restricted to slightly lossy soils and shallowly-buried low-contrast dielectric targets, indicate that, for calibrated ranges of problem parameters, sufficiently accurate and robust target reconstructions can be obtained with reasonable computing times and resources, even with sparse and corrupted data and imperfect knowledge of soil parameters. The proposed approach grants physical insight into the interface/target interaction mechanism, and looks promising from both the computational and accuracy viewpoints, with potential application to antipersonnel land mine clearance. In this connection, the necessary extension to more realistic 3-D configurations, currently under investigation, is fairly straightforward theoretically, but its computational features remain to be explored. Also under investigation are more robust strategies for background field removal.

REFERENCES

[1] "Detection and remediation technologies for mines and minelike targets VI," in *Proc. SPIE*, vol. 4394, A. C. Dubey, J. F. Harvey, J. T. Broach, and V. George, Eds., Oct. 2001.

[2] T. Dogaru and L. Carin, "Time-domain sensing of targets buried under a rough air-ground interface," *IEEE Trans. Antennas Propagat.*, vol. 46, pp. 360–372, Mar. 1998.

[3] R. A. Weisenseel, W. C. Karl, D. A. Castañon, E. L. Miller, C. M. Rappaport, and C. A. DiMarzio, "Statistical fusion of GPR and EMI data," in *Proc. Detection and Remediation Technologies for Mines and Minelike Targets IV*, vol. 3710, Proc. SPIE, A. C. Dubey, J. F. Harvey, J. Broach, and R. E. Dugan, Eds., Aug. 1999, pp. 1179–1187.

[4] T. Dogaru, L. Collins, and L. Carin, "Optimal time-domain detection of a deterministic target buried under a randomly rough interface," *IEEE Trans. Antennas Propagat.*, vol. 49, pp. 313–326, Mar. 2001.

[5] H. Zhan, C. M. Rappaport, M. El-Shenawee, and E. L. Miller, "Mine detection under rough ground surfaces using 2-D FDTD modeling and hypothesis testing," in *Proc. IEEE Antennas Propagat. Int. Symp.*, vol. 3, Boston, MA, July 8–13, 2001, p. 756.

[6] H. Feng, D. A. Castañon, W. C. Karl, and E. L. Miller, "GPR imaging approaches for buried plastic landmine detection," in *Proc. Detection and Remediation Technologies for Mines and Minelike Targets V*, vol. 4038, Proc. SPIE, A. C. Dubey, J. F. Harvey, J. T. Broach, and E. R. Dugan, Eds., Aug. 2000, pp. 1485–1496.

[7] J. J. Maciel and L. B. Felsen, "Systematic study of fields due to extended apertures by Gaussian beam discretization," *IEEE Trans. Antennas Propagat.*, vol. 37, pp. 884–892, July 1989.
[8] ——, "Gaussian beam analysis of propagation from an extended aperture distribution through dielectric layers, part I—plane layer," *IEEE Trans. Antennas Propagat.*, vol. 38, pp. 1607–1617, Oct. 1990.
[9] ——, "Gaussian beam analysis of propagation from an extended aperture distribution through dielectric layers, part II—circular cylindrical layer," *IEEE Trans. Antennas Propagat.*, vol. 38, pp. 1618–1624, Oct. 1990.
[10] V. Galdi, L. B. Felsen, and D. A. Castañon, "Quasi-ray Gaussian beam algorithm for time-harmonic two-dimensional scattering by moderately rough interfaces," *IEEE Trans. Antennas Propagat.*, vol. 49, pp. 1305–1314, Sept. 2001.
[11] ——, "Quasi-ray Gaussian beam algorithm for short-pulse two-dimensional scattering by moderately rough dielectric interfaces," *IEEE Trans. Antennas Propagat.*, vol. 51, pp. 171–183, Feb. 2003.
[12] V. Galdi, D. A. Castañon, and L. B. Felsen, "Multifrequency reconstruction of moderately rough interfaces via quasi-ray Gaussian beams," *IEEE Trans. Geosci. Remote Sensing*, vol. 40, pp. 453–460, Feb. 2002.
[13] V. Galdi, J. Pavlovich, W. C. Karl, D. A. Castañon, and L. B. Felsen, "Moderately rough dielectric interface reconstruction via short-pulse quasi-ray Gaussian beams," *IEEE Trans. Antennas Propagat.*, vol. 51, pp. 672–677, Mar. 2003.
[14] V. Galdi, H. Feng, D. A. Castañon, W. C. Karl, and L. B. Felsen, "Multifrequency subsurface sensing in the presence of a moderately rough air-soil interface via quasi-ray Gaussian beams," *Radio Sci.*, vol. 38, no. 2, 2003.
[15] W. C. Chew, *Waves and Fields in Inhomogeneous Media*. Oxford, U.K.: Oxford Press, 1996.
[16] J. B. Keller, "Accuracy and validity of the Born and Rytov approximations," *J. Opt. Soc. Am.*, vol. 59, no. 8, pp. 1003–1004, Aug. 1969.
[17] T. M. Habashy, R. W. Groom, and B. R. Spies, "Beyond the Born and Rytov approximation: a nonlinear approach to electromagnetic scattering," *J. Geophys. Res.*, vol. 98, no. B2, pp. 1759–1775, Feb. 1993.
[18] N. Dasgupta, N. Geng, T. Dogaru, and L. Carin, "On the extended-Born technique for scattering from buried dielectric targets," *IEEE Trans. Antennas Propagat.*, vol. 47, pp. 1739–1743, Nov. 1999.
[19] Y. M. Wang and W. C. Chew, "An iterative solution of the two-dimensional inverse scattering problem," *Int. J. Imaging Syst. Technol.*, vol. 1, pp. 100–108, 1989.
[20] W. C. Chew and Y. M. Wang, "Reconstruction of two-dimensional permittivity distribution using the distorted Born iterative method," *IEEE Trans. Medical Imaging*, vol. 9, pp. 218–225, June 1990.
[21] W. H Press, S. A. Teukolsky, W. T. Vetterling, and B. P. Flannery, *Numerical Recipes in C: The Art of Scientific Computing*, 2nd ed. Cambridge, U.K.: Cambridge Univ. Press, 1992.
[22] M. Bertero, "Linear inverse and ill-posed problems," in *Advances in Electronics and Electron Physics*. San Diego, CA: Academic Press, 1989, vol. 75, pp. 1–20.
[23] A. J. Devaney, "A filtered backpropagation algorithm for diffraction tomography," *Ultrason. Imag.*, vol. 4, no. 4, pp. 336–349, Oct. 1982.
[24] T. Melamed, Y. Ehrlich, and E. Heyman, "Short-pulse inversion of inhomogeneous media: a time-domain diffraction tomography," *Inverse Problems*, vol. 12, no. 6, pp. 977–993, Dec. 1996.
[25] R. C. Gonzales and R. E. Woods, *Digital Image Processing*. New York: Addison Wesley, 1993.
[26] C. R. Vogel and M. E. Oman, "Fast, robust total variation-based reconstruction of noisy, blurred images," *IEEE Trans. Image Processing*, vol. 7, pp. 813–824, June 1998.
[27] D. C. Dobson and F. Santosa, "An image-enhanced technique for electrical impedance tomography," *Inverse Problems*, vol. 10, no. 2, pp. 317–334, Apr. 1994.
[28] P. van den Berg and R. E. Kleinman, "A total variation enhanced modified gradient algorithm for profile reconstruction," *Inverse Problems*, vol. 13, no. 6, pp. 1607–1620, Dec. 1997.
[29] W. C. Karl, "Regularization in image restoration and reconstruction," in *Handbook of Image and Video Processing*, A. Bovik, Ed. New York: Academic Press, 2000, pp. 141–160.
[30] J. Kaufhold, R. C. Chan, W. C. Karl, and D. A. Castañon, "Ultrasound tissue analysis and characterization," in *Battlefield Biomedical Technologies*, vol. 3712, Proc. SPIE, H. H. Pien, Ed., July 1999, pp. 73–83.
[31] A. N. Tikhonov and V. Y. Arsenin, *Solution of Ill-Posed Problems*. Washington, D.C.: V. H. Winston, 1977.
[32] P. C. Hansen, "Analysis of discrete ill-posed problems by means of the L-curve," *SIAM Rev.*, vol. 34, no. 4, pp. 561–580, Dec. 1992.
[33] A. Yezzi, S. Kichenassamy, K. Kumar, P. Olver, and A. Tennenbaum, "A geometric snake model for segmentation of medical imagery," *IEEE Trans. Medical Imaging*, vol. 16, pp. 199–209, Apr. 1997.
[34] J. Shah, "Riemannian drums, anisotropic curve evolution, and segmentation," *J. Visual Communicat. Image Representation*, vol. 11, no. 2, pp. 142–153, June 2000.
[35] A. Litman, D. Lesselier, and F. Santosa, "Reconstruction of a two-dimensional binary obstacle by controlled evolution of a level set," *Inverse Problems*, vol. 14, no. 3, pp. 685–706, June 1998.
[36] O. Dorn, E. L. Miller, and C. M. Rappaport, "A shape reconstruction method for electromagnetic tomography using adjoint fields and level sets," *Inverse Problems*, vol. 16, no. 5, pp. 1119–1156, Oct. 2000.
[37] H. Feng, W. C. Karl, and D. A. Castañon, "A curve evolution approach to object-based tomographic reconstruction," *IEEE Trans. Image Processing*, vol. 12, pp. 44–57, Jan. 2003.
[38] S. Osher and J. Sethian, "Fronts propagation with curvature dependent speed: algorithms based on Hamilton-Jacobi formulations," *J. Comp. Phys.*, vol. 79, no. 1, pp. 12–49, Nov. 1988.
[39] F. Santosa, "A level-set approach for inverse problems involving obstacles," *ESAIM: Control, Optimization, and Calculus of Variations*, vol. 1, pp. 17–33, 1996.
[40] Y. Leviatan and A. Boag, "Analysis of electromagnetic scattering from dielectric cylinders using a multifilament current model," *IEEE Trans. Antennas Propagat.*, vol. 35, pp. 1119–1127, Oct. 1987.
[41] J. E. Hipp, "Soil electromagnetic parameters as functions of frequency, soil density, and soil moisture," *Proc. IEEE*, vol. 62, pp. 98–103, Jan. 1974.

Vincenzo Galdi (M'98) was born in Salerno, Italy, on July 28, 1970. He received the *Laurea* degree (*summa cum laude*) in electrical engineering and the Ph.D. degree in applied electromagnetics from the University of Salerno, Italy, in 1995 and 1999, respectively.

From April to December 1997, he held a visiting position in the Radio Frequency Division of the European Space Research & Technology Centre (ESTEC-ESA), Noordwijk, The Netherlands. From September 1999 to August 2002, he held a research associate position in the Department of Electrical and Computer Engineering at Boston University, Boston, MA. In September 2002, he was appointed Associate Professor of Electromagnetics, and joined the Department of Engineering at the University of Sannio, Benevento, Italy, where he is currently working. His research interests include analytical and numerical techniques for wave propagation in complex environments, electromagnetic chaos, and inverse scattering.

Dr. Galdi is a Mmber of Sigma Xi. He is the recipient of a 2001 International Union of Radio Science (URSI) "Young Scientist Award."

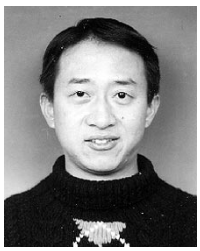

Haihua Feng (M'02) was born in Ningbo, China, in 1973. He received the B.S. degree in applied physics and the B.S. degree in computer science (with distinction) from Shanghai Jiao Tong University, Shanghai, China, in 1995. He received the M.S. and Ph.D. degrees both in electrical engineering from Boston University, Boston, MA, in 1999 and 2002, respectively. His dissertation was entitled "Curve evolution object-based techniques for image reconstruction and segmentation."

From 1997 to 1999, he worked in the Multi-Dimensional Signal Processing Laboratory, Boston University, as a Research Assistant. In May 2000, he joined The MathWorks, Incorporated, Natick, MA, as a Software Engineer and is currently working in the Simulink/Real-Time-Workshop group. His research interests include curve/surface evolution theory, inverse problems, underground imaging, image segmentation and medical imaging. He is also interested in developing model-based simulation and real-time code generation techniques for DSP and Communications systems.

David A. Castañon (S'68–M'79–SM'98) received the B.S. degree in electrical engineering from Tulane University, New Orleans, LA, in 1971, and the Ph.D. degree in applied mathematics from the Massachusetts Institute of Technology (MIT), Cambridge, MA, in 1976.

From 1976 to 1981, he was a Research Associate with the Laboratory for Information and Decision Systems at MIT. From 1982 to 1990, he was Senior and Chief Research Scientist at Alphatech, Incorporated, Burlington, MA. Since 1990, he has been a Professor in the Department of Electrical and Computer Engineering at Boston University, Boston, MA. His research interests include stochastic control and estimation, optimization, and image processing.

Dr. Castañon is a Member of the American Mathematical Society, (AMS) Providence, RI, Soceity for Industrial and Applied Mathematics (SIAM) Philadelphia, PA, and Institute for Operations Research and the Management Sciences (INFORMS), Linthicum, MD. He served as a Member of the Board of Governors of the IEEE Control Systems Society.

William Clem Karl (M'91–SM'00) received the Ph.D. degree in electrical engineering and computer science in 1991 from the Massachusetts Institute of Technology, Cambridge, where he also received the S.M., E.E., and S.B. degrees.

He held the position of Staff Research Scientist with the Brown-Harvard-M.I.T. Center for Intelligent Control Systems and the M.I.T. Laboratory for Information and Decision Systems from 1992 to 1994. He joined the faculty of Boston University in 1995, where he is currently Associate Professor of Electrical and Computer Engineering. Since January 1996, he has also held a joint appointment in the Department of Biomedical Engineering at Boston University. His research interests are in the areas of multidimensional and multiscale signal and image processing, geometric estimation, detection, and medical signal and image processing.

Dr. Karl is a Member of Sigma Xi. He has been an Associate Editor of the IEEE TRANSACTIONS ON IMAGE PROCESSING. He has also served in various organizational capacities, including Session Organizer and Chair for the 36th Asilomar Conference on Signals, Systems and Computers, special session on Inverse Problems in Imaging and 2000 Conference in Information Sciences and Systems special session on Medical Imaging. He was part of the organizing committee for the First SIAM Conference on the Life Sciences.

Leopold B. Felsen (S'47–M'54–SM'55–F'62–LF'90) was born in Munich, Germany, on May 7, 1924. He received the B.E.E., M.E.E, and D.E.E. degrees from the Polytechnic Institute of Brooklyn, Brooklyn, NY, in 1948, 1950, and 1952, respectively.

He emigrated to the United States in 1939 and served in the U.S. Army from 1943 to 1946. After 1952, he remained with the Polytechnic (now Polytechnic University), gaining the position of University Professor in 1978. From 1974 to 1978, he was Dean of Engineering. In 1994, he resigned from the full-time Polytechnic faculty and was granted the status of University Professor Emeritus. He is now Professor of Aerospace and Mechanical Engineering and Professor of Electrical and Computer Engineering at Boston University, Boston, MA (part-time). He is the author or coauthor of over 350 papers and of several books, including the classic *Radiation and Scattering of Waves* (Piscataway, NJ: IEEE Press, 1994). He is an Associate Editor of several professional journals and an Editor of the *Wave Phenomena Series* (New York: Springer-Verlag). His research interests encompass wave propagation and diffraction in complex environments and in various disciplines, high-frequency asymptotic and short-pulse techniques, and phase-space methods with an emphasis on wave-oriented data processing and imaging.

Dr. Felsen is a member of Sigma Xi and a Fellow of the Optical Society of America and the Acoustical Society of America. He has held named Visiting Professorships and Fellowships at universities in the United States and abroad, including the Guggenheim in 1973 and the Humboldt Foundation Senior Scientist Award in 1981. In 1974, he was an IEEE Antennas and Propagation Society Distinguished Lecturer. His Poet's Corner appears sporadically in the IEEE ANTENNAS AND PROPAGATION MAGAZINE. He received the IEEE Antennas and Propagation Society's Best Paper Award for 1969, and was coauthor for 1974, 1981; he was contributing author to papers selected for the R. W. P. King Award for 1884, 1986, and 2000. Moreover, he received the Balthasar van der Pol Gold Medal from the International Union of Radio Science (URSI) in 1975, an honorary doctorate from the Technical University of Denmark in 1979, an IEEE Centennial Medal in 1984, the IEEE Heinrich Hertz Gold Medal for 1991, the Antennas and Propagation Society's Distinguished Achievement Award for 1998, the IEEE Third Millenium Medal in 2000 (nomination by APS), the IEEE Electromagnetics Award for 2003, and three Distinguished Faculty Alumnus Awards from Polytechnic University. In 1977, he was elected to the National Academy of Engineering. He has served on the APS Administrative Committee from 1963–1966, and was Vice Chairman and Chairman for both the United States (1966–1973) and the International (1978–1984) URSI Commission B.